

Note: This work has not yet been peer-reviewed and is provided by the contributing author(s) via EarthArXiv.org as a means to ensure timely dissemination of scholarly and technical work on a noncommercial basis. Copyright and all rights therein are maintained by the author(s) or by other copyright owners. It is understood that all persons copying this information will adhere to the terms and constraints invoked by each author's copyright. This work may not be reposted without explicit permission of the copyright owner.

This work is under review at the *Journal of Physical Oceanography*. Copyright in this work may be transferred without further notice.

Abyssal Circulation Driven By Near-Boundary Mixing:

Water Mass Transformations and Interior Stratification

Henri F. Drake* and Raffaele Ferrari

Massachusetts Institute of Technology, Cambridge, Massachusetts.

Jörn Callies

California Institute of Technology, Pasadena, California.

⁸ **Corresponding author address:* Henri F. Drake, Department of Earth, Atmospheric, and Planetary
⁹ Sciences, Massachusetts Institute of Technology, 77 Massachusetts Ave, Cambridge, MA 02139.
¹⁰ E-mail: henrifdrake@gmail.com

ABSTRACT

11 The emerging view is that the abyssal circulation is forced by bottom-
12 enhanced mixing, which forces downwelling in the stratified ocean interior
13 and upwelling in a bottom boundary layer along an insulating and sloping
14 seafloor. In the limit of slowly-varying vertical stratification and topogra-
15 phy, however, boundary layer theory predicts these up- and down-slope flows
16 largely compensate, such that net watermass transformations along the slope
17 are vanishingly small. Using a Planetary-Geostrophic Circulation Model that
18 resolves both the boundary-layer dynamics and the large-scale overturning
19 in an idealized basin with bottom-enhanced mixing along a mid-ocean ridge,
20 we show that vertical variations in stratification become sufficiently large at
21 equilibrium to reduce the degree of compensation along the mid-ocean ridge
22 flanks. The resulting large net transformations are similar to estimates for the
23 abyssal ocean and span the vertical extent of the ridge. At the base of the
24 slope, the simulated net transformation is well-predicted by upwelling in the
25 bottom boundary layer and independent of the vertical stratification. These
26 results suggest that boundary flows generated by mixing play a crucial role in
27 setting the global ocean stratification and overturning circulation, requiring a
28 revision of abyssal ocean theories.

29 **1. Motivation**

30 The abyssal ocean, below 2500 m, is a massive reservoir for climatically active tracers such
31 as carbon and heat. The rates at which heat is mixed and advected into the high capacity abyssal
32 ocean are key parameters in understanding both past climate reconstructions (e.g. Toggweiler et al.
33 1989) and future projections of climate change (e.g. Hansen et al. 1985). Similarly, the partitioning
34 of carbon between the deep ocean and the atmosphere is a major factor on millennial-scale climate
35 change, whether natural (e.g. Sarmiento and Toggweiler 1984) or anthropogenic in origin (Archer
36 et al. 1998). It is thus vital to have a firm phenomenological and dynamical understanding of the
37 abyssal ocean's mean state.

38 The general structure of the abyssal ocean circulation is easily inferred from surface buoyancy
39 fluxes and large-scale tracer properties (Sverdrup et al. 1942). Antarctic Bottom Waters, the dens-
40 est oceanic waters, form in the Southern Ocean and fill the global abyssal oceans up to a depth
41 of about 2500 m (Talley 2013a). They outcrop at the surface only in the Southern Ocean, where
42 they experience a significant area-integrated buoyancy loss (Abernathey et al. 2016) and are con-
43 verted back into lighter waters by a diabatic abyssal overturning circulation of $O(15 \text{ Sv})$, where
44 $1 \text{ Sv} = 10^6 \text{ m}^3 \text{ s}^{-1}$. This abyssal overturning is believed to be primarily driven by mechanical mix-
45 ing (Lumpkin and Speer 2007). Non-linearities in the equation of state of seawater and geothermal
46 heating at the seafloor are thought to play secondary roles in shaping this circulation and will be
47 ignored in the conceptual models described below (Emile-Geay and Madec 2009; de Lavergne
48 et al. 2016).

49 Classical theories for the abyssal ocean describe the steady state circulation and stratification of
50 a flat-bottom ocean forced by uniform turbulent mixing (Stommel 1957; Robinson and Stommel
51 1959; Stommel and Arons 1959b,a; Munk 1966). These theories remain pedagogically useful,

52 but are at best qualitative descriptions, as demonstrated for example by the fact that the direction
53 of the flow in the Stommel and Arons (1959b) solution changes sign when a realistic seafloor
54 slope is introduced (Rhines 1993) and that the Munk (1966) solution does not satisfy the no-
55 flux boundary condition at the sloping seafloor. The classical Munk (1966) view of a uniform
56 mixing-driven upwelling is further challenged by the observation that turbulent mixing is typically
57 bottom-enhanced over rough topography, reversing the sign of the vertical flow implied by the
58 interior ocean vertical density balance (Polzin et al. 1997; Ferrari et al. 2016).

59 In the ensuing years, several approaches were taken to address the limitations of classical theo-
60 ries. First, boundary layer theories (Wunsch 1970; Thorpe 1987; Garrett 1990) arose to elucidate
61 the local behavior of mixing-induced flow along a sloping and insulating sea floor. Second, the
62 limitations of the Stommel and Arons (1959b) theory inspired a number of extensions to the the-
63 ory to account for baroclinic structure (Kawase 1987; Pedlosky 1992), non-uniform seafloor depth
64 (Rhines 1993), and/or non-uniform turbulent diffusivities κ (Marotzke 1997; Samelson 1998).
65 Third, the observation of bottom-enhanced mixing motivated the development of progressively
66 more sophisticated parameterizations of vertical (or diapycnal) turbulent diffusivities (Bryan and
67 Lewis 1979; St. Laurent and Garrett 2002; Polzin 2009) which were subsequently implemented
68 into general circulation models (Huang and Jin 2002; Jayne 2009; Melet et al. 2016). Fourth, the
69 conundrum of interior downwelling implied by bottom-enhanced mixing was resolved by apply-
70 ing the watermass transformation framework to a downwelling interior layer of turbulent buoyancy
71 flux divergence and an upwelling bottom boundary layer of turbulent buoyancy flux convergence,
72 respectively (Ferrari et al. 2016; McDougall and Ferrari 2016). Despite the direct relevance of all
73 of these approaches to the abyssal circulation, there has been little work done to unify them into a
74 general theory of the abyssal circulation and stratification.

75 Building on the framework introduced by Callies and Ferrari (2018), we present a unified prog-
76 nostic model of the circulation in an abyssal basin forced by bottom-enhanced mixing along a
77 mid-ocean ridge. We modify the geometry, buoyancy forcing, and initial condition of the Callies
78 and Ferrari (2018) model to include the effects of a rough mid-ocean ridge and a non-uniform
79 background stratification on the circulation. Our approach is to formulate the simplest possible
80 model which represents what we believe to be the key aspects of the problem: 1) the transforma-
81 tion of abyssal bottom waters into relatively lighter deep waters by bottom-enhanced mixing on the
82 flanks of a mid-ocean ridge, 2) frictional processes acting on boundary currents, 3) restratification
83 of bottom mixing layers by baroclinic turbulence, and 4) bottom water formation in the South-
84 ern Ocean. The key dynamics that emerge are: 1) mixing layer flows along the mid-ocean ridge
85 and 2) an interhemispheric meridional overturning circulation consisting of layered deep western
86 boundary currents. The unified model incorporates the key concepts from the various approaches
87 described above.

88 The general structure of the abyssal circulation that emerges from the model consists of layered
89 deep western boundary currents along the western continental slope which are connected by zonal
90 flows to watermass transformations driven by bottom-enhanced mixing along a mid-ocean ridge,
91 as schematized in Figure 1. The evolution of the interior stratification and the mixing layer wa-
92 termass transformations are coupled by slope-normal exchange flows, with the vertically-varying
93 equilibrium stratification being determined by a combination of the mixing layer dynamics and a
94 buoyancy restoring applied in the south. Finite net watermass transformations arise ubiquitously
95 along the flanks of the mid-ocean ridge, supported by vertical variations in the interior stratifi-
96 cation, such that the crest of the mid-ocean ridge determines the vertical extent of the abyssal
97 overturning cell, in contrast to a previous constant-stratification interpretation in which finite net
98 transformations are confined to the base of topographic slopes (Callies and Ferrari 2018).

99 The paper is structured as follows. Section 2 reviews the results of several theories of abyssal
100 stratification and circulation in the literature. Section 3 presents the formulation of the Planetary
101 Geostrophic Circulation Model (PGCM) used to produce most of the simulation results presented
102 in the paper. Section 4 describes the general structure of the abyssal circulation as it emerges in
103 the PGCM. In Section 5 we use local solutions to the one-dimensional boundary layer equations to
104 emulate the three-dimensional abyssal circulation in the PGCM. Section 6 describes the spin-up to
105 equilibrium of the vertical structure of abyssal interior stratification and its influence on watermass
106 transformations. Section 7 compares watermass transformations in our PGCM simulations with
107 estimates for the mid-ocean ridges of the Pacific, Atlantic, and Indian Ocean basins. Section 8
108 compares diagnostic estimates of abyssal upwelling from the watermass transformation framework
109 with the classic vertical advection-diffusion framework. Section 9 discusses the implications of
110 our results, some key caveats, and some promising future directions.

111 **2. Theoretical Background**

112 *a. Classical theories of abyssal stratification and circulation*

113 Theories of the abyssal circulation begin with a series of papers by Stommel and Arons
114 (1959b,a). In their theory, the circulation of a homogeneous abyssal layer is fed by high-latitude
115 sources of abyssal water (diabatic downwelling) and driven by a uniformly-distributed sink (di-
116 abatic upwelling) of abyssal water. A uniform upwelling across the base of the thermocline is
117 prescribed, inspired by the thermocline-thermohaline theory of Robinson and Stommel (1959).
118 Munk (1966) further simplifies the Robinson and Stommel (1959) balance by restricting his at-
119 tention to the deep ocean (i.e. below the thermocline) and considering only vertical advection and

120 diffusion,

$$u^z b_z = \partial_z (\kappa b_z), \quad (1)$$

121 where b is buoyancy, u^z is a uniform vertical velocity, κ is a uniform turbulent diffusivity, and
122 subscripts denote partial derivatives. The Munk formulation allows exponential solutions that can
123 be fitted to the observed temperature distributions to yield the canonical estimate of deep ocean
124 mixing $\kappa \simeq 10^{-4} \text{ m}^2\text{s}^{-1}$ for a uniform upwelling of $u^z = 1.4 \times 10^{-7} \text{ m/s}$.

125 The horizontal abyssal circulation associated with the upwelling is described by Stommel and
126 Arons (1959b,a): interior flow is geostrophically-balanced and its meridional component u^y is
127 driven by vortex stretching, as shown by the vertically-integrated planetary-geostrophic vorticity
128 balance

$$\beta U^y = f \frac{u_0^z}{H}, \quad (2)$$

129 where H is the thickness of the abyssal layer, $u_0^z > 0$ is the upwelling across the base of the
130 thermocline, f is the Coriolis parameter, $\beta > 0$ is the meridional gradient of the Coriolis parameter,
131 and the vertically-integrated flow U^y is thus poleward in both hemispheres (see Pedlosky 1996
132 for an elucidating derivation). Inspired by the success of analogous theories for the wind-driven
133 gyre circulation (Stommel 1948), Stommel and Arons (1959b,a) suppose the existence of a deep
134 western boundary current in which arbitrary frictional effects allow the current to deviate from
135 geostrophy and arrange itself to match the interior flow and such that the abyss conserves mass.

136 *b. Turning ocean mixing upside down*

137 The Stommel and Arons (1959b,a) and Munk (1966) theories for abyssal circulation and strati-
138 fication described above rely on the existence of a uniform turbulent diffusivity $\kappa \simeq 10^{-4} \text{ m}^2\text{s}^{-1}$,
139 roughly an order of magnitude smaller than the interior ocean mixing inferred from observations
140 (Gregg 1989; Ledwell et al. 1993). While sufficiently vigorous mixing was eventually discovered

141 deeper in the ocean near rough seafloor topography (Polzin et al. 1997; Ledwell et al. 2000), the
 142 abyssal mixing problem only became more complicated: applying the vertical advection-diffusion
 143 balance (eq.1) point-wise to the bottom-enhanced mixing profiles $\kappa(z)b_z \simeq \Gamma\varepsilon$, where $\Gamma \simeq 0.2$ is
 144 the mixing efficiency and ε is the measured dissipation rate, implies diapycnal *downwelling*

$$u^z = b_z^{-1} \partial_z (\kappa b_z) < 0, \quad (3)$$

145 in contrast to the diapycnal *upwelling* required to balance diapycnal downwelling at high latitudes
 146 (Stommel and Arons 1959b,a; Munk 1966)!

147 This apparent conundrum is resolved by considering the insulating boundary condition at a
 148 sloping seafloor, which causes buoyancy convergence and hence diapycnal upwelling in a thin
 149 bottom boundary layer (Polzin et al. 1997; Ferrari et al. 2016). In this framework, the abyssal
 150 overturning is the net effect of downwelling driven by bottom-enhanced mixing in a stratified
 151 mixing layer and upwelling driven by buoyancy convergence in a bottom boundary layer, which
 152 we collectively refer to as bottom mixing layers (Callies and Ferrari 2018).

153 *c. A puzzling constraint from boundary layer theory*

154 Bottom boundary layer theory (e.g. Garrett et al. 1993) is a useful dynamical approach to the
 155 problem of flow driven by near-boundary mixing on a slope, which exerts a strong control on the
 156 basin-scale abyssal circulation (Callies and Ferrari 2018). Following Thorpe (1987), who built
 157 on the approaches of Wunsch (1970) and Phillips (1970), we rotate the Boussinesq equations into
 158 slope coordinates and assume the flow depends only on the slope-normal coordinate z' , which
 159 gives the simplified buoyancy equation (see derivation of full equation set in Section 5a):

$$b'_t + u^x N_0^2 \sin \theta = \partial_{z'} [\kappa (N_0^2 \cos \theta + b'_{z'})] \quad (4)$$

160 where $u^{x'}$ is the up-slope velocity, κ the turbulent diffusivity, θ the slope angle, $\kappa = \kappa(z')$ the
 161 turbulent diffusivity, and we decompose the buoyancy field $b(x, y, z) = N_0^2 z + b'(x, y, z)$ into a back-
 162 ground corresponding to a constant stratification N_0^2 and a buoyancy anomaly $b' = b'(z')$. The
 163 boundary conditions are a no-flux condition $b_{z'} = b'_{z'} + N_0^2 \cos \theta = 0$ at the seafloor $z' = 0$ and de-
 164 cay conditions $u^{x'}, b'_{z'} \rightarrow 0$ as $z' \rightarrow \infty$. At steady state, the boundary layer equation for the buoyancy
 165 anomaly (eq. 4) can be integrated from $z' = 0$ to $z' \rightarrow \infty$, which yields

$$\Psi_{\text{bg}} \equiv \kappa_{\text{bg}} \cot \theta, \quad (5)$$

166 for the net up-slope transport per unit length $\Psi_{\text{bg}} = \int_0^\infty u^{x'} dz'$, where $\kappa_{\text{bg}} \equiv \kappa(z \rightarrow \infty)$ is the
 167 background diffusivity. The simplicity of this integral constraint is surprising: the net up-slope
 168 transport depends only on the background turbulent diffusivity κ_{bg} and the slope angle θ , and is
 169 independent of other environmental parameters which might be expected to influence diapycnal
 170 transport, such as frictional parameters, the background stratification N_0^2 , the Coriolis parameter
 171 f , and the vertical structure of the turbulent diffusivity $\kappa(z)$. Since $b'(z')$ is always a monotonic
 172 function, the net up-slope and net diapycnal transport are equivalent, and we hereafter use the two
 173 terms interchangeably.

174 Integrating the prediction Ψ_{bg} for the diapycnal transport per unit length along the perimeter
 175 $L_{\text{global}} \simeq 10^8$ m of the global mid-ocean ridge system (Callies 2018) for a typical ridge slope
 176 $\tan(\theta) = 2 \times 10^{-3}$ and a background diffusivity of $\kappa_{\text{bg}} < 10^{-5} \text{ m}^2\text{s}^{-1}$ produces a global mixing-
 177 driven diapycnal overturning transport of $L_{\text{global}} \kappa_{\text{bg}} \cot \theta < 0.5$ Sv, more than an order of magni-
 178 tude smaller than the observed abyssal diapycnal overturning transport of roughly 15 Sv (Lumpkin
 179 and Speer 2007).

180 Callies and Ferrari (2018) resolve this conundrum by using the magnitude of the upwelling-
 181 downwelling ‘dipole’ from boundary layer theory as a prediction for the net watermass transfor-

182 mation, since at the base of topographic slopes the in- and outflows into the boundary layers occur
 183 at different density classes and thus drive a diabatic overturning. They find that the strictly up-
 184 welling transport in the bottom boundary layer accurately predicts the scaling of the maximum net
 185 diapycnal overturning transport, although the predicted overturning is unrealistically confined to
 186 the base of topographic slopes where the constraints from one-dimensional boundary layer theory
 187 break down.

188 *d. Boundary-interior exchange*

189 The integral constraint $\Psi_{\text{bg}} \equiv \kappa_{\text{bg}} \cot \theta$ (eq. 5) relies on the assumption of constant background
 190 stratification N_0^2 . By construction, none of the other terms are assumed to vary in the plane of the
 191 slope (x', y') either; it follows that there are no cross-slope convergences $\partial_{x'} u^{x'} = 0$ and hence no
 192 slope-normal exchange between the bottom mixing layers and the interior, $u^{z'} = 0$ (Wunsch 1970).

193 With a vertically varying stratification $N^2(z)$, however, variations in the buoyancy gradient
 194 project onto the cross-slope direction $x' = x \cos \theta + z \sin \theta$, introducing a second dimension to
 195 the problem (e.g. Phillips et al. 1986; Salmun et al. 1991) and permitting both slope-normal ex-
 196 change flows $u^{z'} \neq 0$ and a net diapycnal transport $\psi_\infty \equiv \int_0^\infty u^{x'} dz' \neq \Psi_{\text{bg}}$. Heterogeneities can also
 197 arise due to cross-slope variations in the turbulent diffusivity $\kappa(x, y, z)$ or the slope angle $\theta(x, y, z)$
 198 (Dell and Pratt 2015; Holmes et al. 2018), though these are small by construction in our idealized
 199 model configuration.

200 *e. Dynamics controlling the interior abyssal stratification*

201 The abyssal stratification is thought to be controlled by the combined effects of 1) diapycnal
 202 mixing in ocean basins; and 2) the competing effects of winds and mesoscale eddies in setting the
 203 slope of isopycnals in the Southern Ocean. Diapycnal mixing maintains the stable stratification

204 of the abyssal ocean by effectively diffusing buoyancy downwards, transforming dense abyssal
205 waters into relatively lighter deep waters (Munk 1966). This vertical advection-diffusion model is
206 an incomplete model of the abyssal stratification, however, as it omits the complementary process
207 which closes the overturning circulation by transforming light deep waters into relatively denser
208 abyssal waters. Theoretical progress on understanding the abyssal stratification slowed until the
209 breakthrough development of quasi-adiabatic theories of Southern Ocean circulation. In these
210 theories, deep waters are upwelled adiabatically along sloping isopycnals in the Southern Ocean,
211 are transformed into abyssal waters in the Southern Ocean mixed layer by a negative surface
212 buoyancy flux, and return to the abyss adiabatically along isopycnals (Marshall and Speer 2012,
213 and references therein). Making use of the Transformed Eulerian Mean approach, one can show
214 that the Southern Ocean isopycnal slope is determined by a balance between wind stress and
215 stirring by mesoscale eddies, which steepen and flatten isopycnals, respectively (Marshall and
216 Radko 2003).

217 Building on these two independent theories, Nikurashin and Vallis (2011) develop an idealized
218 model which couples quasi-adiabatic Southern Ocean dynamics to a diabatic abyssal ocean basin
219 and predicts the abyssal stratification and circulation, given only surface boundary conditions and
220 mixing coefficients. For moderate diapycnal mixing of $10^{-5} \text{ m}^2\text{s}^{-1} < \kappa < 10^{-3} \text{ m}^2\text{s}^{-1}$, a regime
221 applicable to both the Ocean and the model described here, the Nikurashin and Vallis (2011) model
222 predicts that the interior abyssal stratification depends both on winds and eddies in the Southern
223 Ocean and diapycnal mixing in the basin.

224 A promising aspect of zonally-integrated models of the meridional overturning circulation (e.g
225 Nikurashin et al. 2012; Thompson et al. 2016) is that they accurately reproduce the overturning
226 and stratification exhibited by idealized “box”-geometry general circulation models. The emerging
227 view, however, is that the abyssal circulation of the ocean is controlled by mixing layer flows along

228 sloping boundaries and thus that the commonly-used “box” geometry models may be a misleading
 229 point of reference for theories of the abyssal stratification and circulation (Ferrari et al. 2016).
 230 Building on Callies and Ferrari (2018), we describe the formulation of an improved idealized
 231 general circulation model in a “bowl + ridge” geometry which accommodates the recent revisions
 232 to our theoretical understanding of the abyssal ocean circulation.

233 **3. Planetary Geostrophic Circulation Model (PGCM)**

234 The numerical model used here is the Planetary Geostrophic Circulation Model (PGCM) de-
 235 veloped by Callies and Ferrari (2018) to study how bottom-enhanced mixing on slopes drives
 236 an abyssal circulation. We describe the key elements of our PGCM configuration below, which
 237 closely follows the exposition of Callies and Ferrari (2018). The main differences between the
 238 present study and Callies and Ferrari (2018) are the inclusion of a mid-ocean ridge, the localization
 239 of vigorous bottom-enhanced mixing to a mid-ocean ridge, and the generalization to vertically-
 240 varying interior stratifications.

241 *a. Equations*

242 The model solves the Navier-Stokes equations under the Boussinesq and planetary-scale
 243 geostrophic approximations, with parameterizations for the frictional and diabatic effects of unre-
 244 solved processes, given by

$$f\mathbf{z} \times \mathbf{u} = -\nabla p + b\mathbf{z} - r(\mathbf{x} + \mathbf{y}) \cdot \mathbf{u}, \quad (6)$$

$$\nabla \cdot \mathbf{u} = 0, \text{ and} \quad (7)$$

$$\frac{\partial b}{\partial t} + \mathbf{u} \cdot \nabla b = \nabla \cdot (\kappa \nabla b) - \lambda(y)(b - B(z)), \quad (8)$$

245 where t is time; $\mathbf{x}, \mathbf{y}, \mathbf{z}$ are unit vectors pointing east, north, and up, respectively; $f = \beta y$ is the
246 linearized Coriolis parameter (β -plane approximation); \mathbf{u} is the velocity vector; p is the pressure
247 divided by a reference density; b is the buoyancy; r is a frictional parameter; $\kappa = \kappa(x, y, z)$ is a
248 spatially-dependent turbulent diffusivity; and $\lambda = \lambda(y)$ is a meridionally-varying restoring rate
249 (see Section 3c). The system of equations (6) - (8), with appropriate initial and boundary condi-
250 tions, yields a self-consistent and prognostic model of abyssal circulation and stratification.

251 The Boussinesq approximation filters out acoustic waves while the planetary-geostrophic ap-
252 proximation filters out gravity waves and geostrophic turbulence. The resulting planetary-
253 geostrophic equations are appropriate for basin-scale oceanic circulations and are the set of equa-
254 tions typically used for idealized studies of the abyssal circulation (e.g Pedlosky 1996, and refer-
255 ences therein) and intermediate-complexity earth system models (Holden et al. 2016, e.g.). While
256 it is computationally and conceptually useful that the planetary-geostrophic equations filter out the
257 effects of fast waves and turbulence, the turbulent fluxes of these relatively small-scale flows are
258 thought to have leading order effects on abyssal bottom mixing layers. We include their qualitative
259 effects in the planetary-geostrophic formulation by way of two idealized parameterizations.

260 First, to include the effects of turbulent mixing produced by the local breaking of internal waves
261 generated by flow over rough topography, we introduce a term for the turbulent buoyancy flux
262 convergence $\nabla \cdot (\kappa \nabla b)$ to the buoyancy equation (e.g. as in St. Laurent and Garrett 2002). The
263 imposed spatially-dependent turbulent diffusivity $\kappa(x, y, z)$ approximates the leading-order spatial
264 structure described by observational estimates¹ (e.g. Polzin et al. 1997; Waterhouse et al. 2014)
265 and is described in detail in Section 3c.

¹Quantitatively similar profiles of turbulent kinetic energy dissipation are reproduced in simulations of internal wave turbulence above rough topography, wherein energy from a geostrophic mean flow (Nikurashin and Ferrari 2009) or the barotropic tide (Nikurashin and Legg 2011) is converted into unstable high-mode internal waves via a cascade of wave-wave interactions.

266 Second, to include the qualitative effects of isopycnal mixing by baroclinic turbulence in re-
 267 stratifying the bottom mixing layers (Callies 2018) and in thickening western boundary currents
 268 (e.g. Stommel 1948), we introduce a dissipative term to the momentum equation. Greatbatch
 269 and Lamb (1990) show that introducing vertical momentum diffusion $\partial_z (v_{\text{eddy}} \mathbf{u}_z)$ to the plane-
 270 tary geostrophic equations with an eddy viscosity $v_{\text{eddy}} = \kappa_{\text{GM}} f^2 / N^2$ is equivalent to introducing
 271 isopycnal diffusion of potential vorticity with an effective isopycnal diffusivity of κ_{GM} (Gent and
 272 McWilliams 1990). Following Salmon (1992), we simplify the dynamics further by using a linear
 273 friction term (Rayleigh drag), $-r(\mathbf{x} + \mathbf{y}) \cdot \mathbf{u}$, which should be thought of as a qualitative stand-in
 274 for the effects of poorly understood mixing layer turbulence (Callies and Ferrari 2018). We scale
 275 the frictional parameter r according to the Greatbatch and Lamb (1990) parameterization,

$$r = \kappa_{\text{GM}} \frac{f^2}{\delta^2 N^2} \approx 1.2 \times 10^{-6} \text{ s}^{-1}, \quad (9)$$

276 where we choose $\delta = 500$ m to be roughly the thickness of the bottom mixing layers observed
 277 in the Brazil Basin (Callies 2018) and typical abyssal values of $\kappa_{\text{GM}} = 300 \text{ m}^2 \text{ s}^{-1}$, $f = 6 \times 10^{-5}$
 278 s^{-1} , and $N^2 = 0.5 \times 10^{-6} \text{ s}^{-1}$. The linear drag parameter is small enough that the frictional terms
 279 are negligible in the interior where the flow is approximately geostrophic and are important only
 280 in ‘inner’ boundary layers (both the deep western boundary currents and the bottom mixing layers
 281 along the mid-ocean ridge) where the horizontal velocities are large (Salmon 1992; Callies and
 282 Ferrari 2018). The choice of $r = 1.2 \times 10^{-6} \text{ s}^{-1}$ gives a non-dimensional value $\hat{r} = \frac{r}{\beta L} = 0.1$ such
 283 that the width of the Stommel and Arons (1959b,a) deep western boundary currents is one-tenth
 284 the domain width (see Section 3d).

285 A more complete theoretical motivation, interpretation, and evaluation of the linear drag as a
 286 parameterization for baroclinic turbulence is outside the scope of this paper and will be the subject
 287 of a forthcoming paper. Callies and Ferrari (2018) varied the frictional parameter r within an order

288 of magnitude and found the strength of the overturning circulation in the PGCM to be relatively
289 insensitive; although not shown here, we find the net watermass transformation at equilibrium to
290 be similarly insensitive to the frictional parameter.

291 *b. Geometry and boundary conditions*

292 We configure the PGCM to approximate the leading-order structure of a typical cross-
293 hemispheric abyssal ocean basin with a rectangular basin of zonal width $L = 3000$ km and merid-
294 itional length $2L = 6000$ km. Our idealized basin contains a mid-ocean ridge caused by seafloor
295 spreading in the middle and is bounded in the west, east, and north by continental slopes (Figure
296 2a). Although the southern region in our configuration ($y < -L/2 = -3000$ km) is also zonally
297 bounded, it should be thought of as a Southern Ocean-like sponge layer. In this southern region,
298 the transformation of deep waters into bottom waters arising from complex circumpolar channel
299 dynamics (e.g. as described in Abernathy et al. 2016) are parameterized by an idealized buoy-
300 ancy restoring forcing which pins the buoyancy field to a reference vertical profile (described in
301 detail in the next Section 3c). The model extends from $z = -2500$ m at the upper boundary to a
302 maximum depth of $z = -5000$ m and should be interpreted as representing only the diabatic lower
303 cell of the meridional overturning circulation. The idealized configuration can be thought to apply
304 locally to the Atlantic, Pacific, and Indian Ocean basins below $z = -2500$ m, which in the present
305 climate are all bounded by topography in the west, east, and north and have roughly meridionally-
306 aligned mid-ocean ridges (e.g. those highlighted in Figure 12). The idealized continental slopes
307 are half-Gaussian and the mid-ocean ridge is Gaussian in the zonal direction and tapers down
308 to zero meridionally in the southern restoring region to allow unconstrained zonal flows to close
309 the circulation of interest in the diffusively-forced basin to the north. The characteristic seafloor
310 slopes of roughly $\tan(\theta_{ridge}) \simeq 2 \times 10^{-3}$ for the mid-ocean ridge and $\tan(\theta_{cont.}) \simeq 1 \times 10^{-3}$ for the

311 continental slope are inspired by the South Atlantic, where the bottom mixing layers and large-
 312 scale abyssal circulation are best constrained by existing observations (Polzin et al. 1997; Ledwell
 313 et al. 2000; St. Laurent et al. 2001; Thurnherr et al. 2005). The PGCM is bounded from above by
 314 assuming isopycnals are flat, i.e. $b = 0$ at $z = -2500$ m, which is approximately valid in all basins
 315 north of the Southern Ocean (Talley 2007; Koltermann et al. 2011; Talley 2013b). The PGCM
 316 is bounded from below by an insulating seafloor, $\mathbf{n} \cdot \nabla b = 0$ at $z = -d(x, y)$, where $d(x, y)$ is the
 317 seafloor depth and \mathbf{n} is the unit vector normal to the boundary.

318 *c. Buoyancy forcing*

319 The abyssal circulation in our model is forced by two competing diabatic terms in the buoyancy
 320 equation: minus the divergence of the turbulent buoyancy flux $-\nabla \cdot (-\kappa \nabla b)$, which has a positive
 321 integral contribution (diapycnal upwelling); and restoring to a reference buoyancy profile $-\lambda(b -$
 322 $B)$, which has a negative integral contribution (diapycnal downwelling). Available potential energy
 323 is produced by parameterized turbulent mixing and converted into kinetic energy via the buoyancy
 324 production term $u^z b$ to drive a planetary-geostrophic abyssal circulation and balance the available
 325 potential energy loss due to restoring.

326 *(i) Turbulent mixing*

327 The prescribed turbulent diffusivity $\kappa = \kappa(x, y, z)$ is everywhere bottom-enhanced with a contri-
 328 bution equal to $\kappa_{\text{bot}} \exp\{-(z + d)/h\}$ over the mid-ocean ridge, where we choose $\kappa_{\text{bot}} = 5 \times 10^{-3}$
 329 m^2s^{-1} and $h = 250$ m to roughly match observations in the Brazil Basin (Figure 11). The bottom-
 330 enhanced contribution to κ is reduced by a factor of 20 to $\frac{\kappa_{\text{bot}}}{20} \exp\{-(z + d)/h\}$ over the con-
 331 tinental slopes to reflect the observed weakness of local wave-driven turbulence over smooth
 332 continental slopes (Figure 11 and Polzin et al. 1997). A uniform weak background diffusivity
 333 $\kappa_{\text{bg}} = \frac{\kappa_{\text{bot}}}{200} = 2.5 \times 10^{-5} \text{m}^2\text{s}^{-1}$ is added to stabilize the numerical solution on the continental

334 slopes, which yields a total diffusivity distribution

$$\kappa(x, y, z) = \kappa_{bg} + \begin{cases} \kappa_{bot} \exp\{-(z + d(x, y))/h\}, & \text{if } L/2 < x < 3L/2 \text{ (mid-ocean ridge)} \\ \frac{\kappa_{bot}}{20} \exp\{-(z + d(x, y))/h\}, & \text{else (continental slopes),} \end{cases} \quad (10)$$

335 with a smoothing function applied over a horizontal distance of $L/10$ near the transitions at $x = L/2$
 336 and $x = 3L/2$. The net effect of this prescribed mixing is to power a diabatically upwelling along
 337 the mid-ocean ridge, where mixing is vigorous.

338 *(ii) Buoyancy restoring in the southern restoring region*

339 The prescribed restoring rate λ is constructed to have a meridional dependence

$$\lambda(y) = \lambda_0 \left[0.5 \left(1 - \tanh \left(\frac{y + L/2}{10L} \right) \right) \right] \quad (11)$$

340 which has a uniform rate $\lambda = \lambda_0 \simeq (10 \text{ years})^{-1}$ in the southern restoring region and vanishes
 341 rapidly outside, $\lambda \rightarrow 0$ as $y > -L/2$. The prescribed restoring rate is comparable to a lateral dif-
 342 fusive timescale $\tau_{SO} = L_{SO}^2 / \kappa_{GM} = \frac{(10^6 \text{ m})^2}{3000 \text{ m}^2 \text{ s}^{-1}} \simeq 10 \text{ years}$, determined for an isopycnal diffusivity
 343 $\kappa_{GM} \simeq 3000 \text{ m}^2 \text{ s}^{-1}$ (Abernathey et al. 2013), and a Southern Ocean of width $L_{SO} \simeq 1000 \text{ km}$.
 344 This restoring rate is much faster than the vertical diffusive timescale which spins up the overturn-
 345 ing circulation $\tau_{mix} = H^2 / \bar{\kappa} \simeq 1000 \text{ years}$, where $H = 2500 \text{ m}$ is the maximum thickness of the
 346 abyssal ocean and $\bar{\kappa} \simeq 10^{-4} \text{ m}^2 \text{ s}^{-1}$ is the volume-weighted mean diffusivity in the basin. Thus,
 347 the stratification in the southern restoring region does not deviate much from the prescribed pro-
 348 file. The net effect of this parameterized buoyancy forcing in the southern restoring region is to
 349 transform deep waters into bottom waters (diabatic downwelling) to balance the transformation of
 350 bottom waters into deep waters (diabatic upwelling) driven by mixing along the mid-ocean ridge
 351 in the basin to the north. In contrast to Callies and Ferrari (2018), we allow the reference buoy-
 352 ancy field $B(z)$ to have vertically-varying stratification $B_z = N^2(z)$, complicating the interpretation

353 of the solution in terms of one-dimensional boundary layer dynamics which assume a constant
 354 interior stratification N_0^2 .

355 *d. Dimensional parameters and scaling*

356 While the PGCM is presented in this paper in dimensional terms, the PGCM is in practice
 357 formulated and implemented non-dimensionally. The following dimensional scales,

$$\begin{aligned}
 L &= 6000 \text{ km} && \text{(basin width),} \\
 H &= 2500 \text{ m}, && \text{(abyssal ocean vertical extent),} \\
 \beta &= 2 \times 10^{-11} \text{ m}^{-1} \text{ s}^{-1}, && \text{(meridional gradient of Coriolis parameter),} \\
 N^2 &= 1.5 \times 10^{-6} \text{ s}^{-2}, && \text{(reference stratification at } z = -2500 \text{ m),} \\
 \kappa_{bot} &= 5 \times 10^{-3} \text{ m}^2 \text{ s}^{-1}, && \text{(diffusivity at the mid-ocean ridge seafloor),} \\
 r &= 1.2 \times 10^{-5} \text{ s}^{-1}, && \text{(frictional parameter),}
 \end{aligned}$$

358 are used to non-dimensionalize the system, with the coordinate transformation

$$x = L\hat{x}, \quad y = L\hat{y}, \quad z = H\hat{z} \quad (12)$$

359 and the substitutions

$$t = \frac{\beta L^3}{N^2 H^2} \hat{t}, \quad b = N^2 H \hat{b}, \quad p = N^2 H^2 \hat{p}, \quad (13)$$

$$u^x = \frac{N^2 H^2}{\beta L^2} \hat{u}^{\hat{x}}, \quad u^y = \frac{N^2 H^2}{\beta L^2} \hat{u}^{\hat{y}}, \quad u^z = \frac{N^2 H^3}{\beta L^3} \hat{u}^{\hat{z}}. \quad (14)$$

360 For reference, the non-dimensional time $\hat{t} = 1$ corresponds to $t = \tau \simeq 10$ years, where $\tau \equiv$
 361 $\beta L^3 / N^2 H^2$. While the basin scale circulation takes a long time $\tau_{\text{mix}} = H^2 / \bar{\kappa} \simeq 1000$ years $\gg \tau$ to
 362 spin up, the bottom mixing layers are spun up on a fast timescale $\tau_{\text{BL}} = q^{-2} / \kappa_{\text{bot}} \simeq 1$ year $\ll \tau$,
 363 where

$$q^{-1} = \sqrt{\frac{\kappa_{\text{bot}}(f^2 + r^2)}{rN^2 \tan^2 \theta}} \simeq 400 \text{ m} \quad (15)$$

364 is the thickness of the mixing layer predicted by 1D theory (Callies and Ferrari 2018), $\kappa_{\text{bot}} =$
 365 $5 \times 10^{-3} \text{ m}^2/\text{s}$ is the diffusivity at the seafloor, and we pick $f = \beta L/2$ at $y = L/2$ as a representative
 366 value of the Coriolis parameter.

367 The non-dimensionalized equations (see Callies and Ferrari 2018) depend only on the non-
 368 dimensional parameters

$$\hat{\alpha} = \frac{H}{L}, \quad \hat{\kappa} = \frac{\kappa \beta L^3}{N^2 H^4}, \quad \hat{r} = \frac{r}{\beta L}. \quad (16)$$

369 $\hat{\alpha}$ is the aspect ratio of the basin; $\hat{\kappa} = \tau/\tau_{\text{mix}}$ is the ratio of the cross-basin propagation timescale
 370 of long Rossby waves (with $f = \beta L$)

$$\tau \equiv L/c_g = L/\frac{\beta L^{-2}}{(NH/f)^2} = \frac{\beta L^3}{N^2 H^2}, \quad (17)$$

371 to the diffusive spin-up timescale $\tau_{\text{mix}} \equiv H^2/\bar{\kappa}$. \hat{r} is the ratio of the Stommel (1948) western
 372 boundary layer width r/β to the basin width L . Since the prescribed κ is spatially-dependent,
 373 the non-dimensional diffusivity $\hat{\kappa}$ inherits its spatial dependence in the numerical implementa-
 374 tion. Scaling κ by its volume-weighted average value $\bar{\kappa}$ gives $\hat{\kappa} = \tau/\tau_{\text{mix}} \simeq 0.01$. Because
 375 the imposed turbulent diffusivity is isotropic, the small aspect ratio $\hat{\alpha} \sim 5 \times 10^{-4}$ results in
 376 a non-dimensionalized horizontal diffusivity many orders of magnitude smaller than the non-
 377 dimensionalized vertical diffusivity. Since this is difficult to implement numerically, we arti-
 378 ficially increase the horizontal diffusivity for numerical stability by increasing the aspect ratio
 379 parameter to $\hat{\alpha} = 0.2$ in the non-dimensional equations, where it only enters in the horizontal dif-
 380 fusion term $\hat{\alpha}^2 [\partial_{\hat{x}}(\hat{\kappa}\hat{b}_{\hat{x}}) + \partial_{\hat{y}}(\hat{\kappa}\hat{b}_{\hat{y}})]$ (Callies and Ferrari 2018). Since the aspect ratio remains
 381 small $\hat{\alpha} = 0.2 \ll 1$, it does not qualitatively effect the results presented here, as evidenced by the
 382 negligible role of horizontal buoyancy fluxes in the watermass transformations (Figure 5).

383 *e. Numerical implementation*

384 In practice, the model is formulated in terrain-following coordinates to accurately resolve the
385 thin mixing-driving flows along the sloped bottom boundary. The numerical implementation is
386 described in the Appendix and in Callies and Ferrari (2018). The base Julia (Bezanson et al. 2017)
387 implementation is available at <https://github.com/joernc/pgcm>. The input files, output files,
388 and post-processing notebooks necessary to replicate the study are available at <https://github.com/hdrake/AbyssalFlow> (currently private but will be made public if accepted for publication).

390 **4. Abyssal Circulation Controlled By Mixing Layer Dynamics**

391 We begin by describing the general structure of the abyssal circulation at equilibrium in the
392 PGCM, i.e. at $\hat{t} = 50$ or $t \simeq 500$ years $\simeq \tau_{\text{mix}}$. The stratification in the PGCM solution presented
393 in this section is restored to an exponential profile with a decay scale of $\delta = 1000$ m (solid red
394 dashed line in Figure 2), which exhibits vertical variations of similar magnitude to those observed
395 the Southern Ocean (black solid line). This is arguably our most realistic simulation of the abyssal
396 ocean and hereafter we refer to it as PGCM-REAL.

397 *a. Bottom Mixing Layers and Deep Western Boundary Currents*

398 Figure 3 (a-c) shows the three Cartesian components of the abyssal flow field along a zonal
399 section 3000 km north of the equator. In the bottom mixing layers spanning both flanks of the
400 mid-ocean ridge, buoyancy surfaces plunge to intersect the seafloor at a right angle (visually dis-
401 torted by the aspect ratio) to satisfy the no-flux boundary condition. As expected from 1D theory
402 (Callies and Ferrari 2018), the boundary flows are relatively thicker and stronger over the mid-
403 ocean ridge where mixing is strong; in contrast, the boundary flows are thin and weak over the
404 continental slopes where mixing is weak. In the bottom boundary layer (BBL), plunging buoy-

405 buoyancy surfaces drive frictionally-balanced upwelling (Figure 3c) and frictional-geostrophic flow
406 opposite the direction of Kelvin wave propagation (Figure 3b), i.e. anti-cyclonic in the north-
407 ern hemisphere. In the stratified mixing layer (SML) just above the BBL, buoyancy surfaces are
408 roughly flat and the bottom-enhanced mixing drives downwelling (Figure 3c), as expected from
409 the vertical advection-diffusion balance (eq. 3) reviewed in Section 2 and revisited in Section 8.

410 A net residual diapycnal upwelling in the Northern Hemisphere can be inferred from the merid-
411 ional flow field at the equator: dense bottom waters flow into the northern hemisphere and rela-
412 tively lighter deep waters flow out (Figure 3e). Since the Coriolis force vanishes at the equator, the
413 buoyant force associated with the bending of buoyancy surfaces to satisfy the bottom-boundary
414 condition can only be balanced by a cross-slope frictional flow (Figure 3d,f) and any along-slope
415 flow associated with the bottom mixing layers vanishes (compare Figure 3e to Figure 3b). The
416 only meridional flow are Stommel (1948)-like deep western boundary currents (DWBC) along
417 the continental slope on the western side of the domain and the eastern flank of the ridge (Figure
418 3e). In this particular configuration, a southward-flowing DWBC develops on the eastern flank
419 of the ridge near its crest and is much weaker than the DWBC on the western continental slope.
420 The southward DWBC on the ridge is relatively intensified in simulations with a taller ridge or
421 wherein the maximum watermass transformation occurs at greater depths due to changes in the
422 stratification (see Section 6).

423 *b. Depth-integrated and Overturning Circulations*

424 The global abyssal circulation is more intuitively visualized by considering the three Cartesian
425 streamfunctions that describe the flow, which we approximate by integrating the u^x , u^y , and u^z

426 velocities in x , y , and z , respectively² (Figure 4). Figure 4a shows the familiar streamfunction
 427 for the meridional overturning circulation (MOC) in the y - z plane, which should be thought of as
 428 corresponding to the lower-cell of the global MOC. This circulation has a strength of about 1.6 Sv
 429 at the equator, with water 1) downwelling diabatically in the southern restoring region, 2) flowing
 430 northwards to fill the abyssal depths, 3) gradually upwelling along the length of the basin, and 4)
 431 returning to the southern restoring region to close the circulation. We note in particular that the
 432 MOC extends all the way from the ocean seafloor to the top of the mid-ocean ridge, in contrast to
 433 the MOC in the Callies and Ferrari (2018) framework, in which significant overturning is confined
 434 to the base of topographic slopes (see Section 6c for a discussion on the role of the ridge height in
 435 setting the vertical extent of the MOC).

436 The up- and down-welling in the bottom mixing layers is evident in the zonal overturning stream-
 437 function in the x - z plane, which shows upwelling in a thin BBL and broader downwelling in the
 438 SML above (Figure 4c). The upwelling in bottom boundary layers is confined to the two flanks
 439 of the mid-ocean ridge, where mixing is vigorous and bottom-enhanced, and is negligible over
 440 the weakly-mixed continental slopes. In this case, the upwelling and downwelling transports are
 441 equal and opposite in strength because the downwelling flow includes both the residual diabatic
 442 upwelling along the ridge as well as the net diabatic downwelling by the relaxation condition
 443 in the southern restoring region. Nonetheless, the zonal overturning streamfunction provides a
 444 qualitative sense of the zonal overturning circulations driven by mixing layer dynamics along the
 445 mid-ocean ridge.

²Integrating the continuity equation in $\frac{\partial u^x}{\partial x} + \frac{\partial u^y}{\partial y} + \frac{\partial u^z}{\partial z} = 0$ along any of the three directions x , y , or z yields an equation of the form
 $\int \left(\frac{\partial u^{x_1}}{\partial x_1} + \frac{\partial u^{x_2}}{\partial x_2} + \frac{\partial u^{x_3}}{\partial x_3} \right) dx_3 = \frac{\partial U^{x_1}}{\partial x_1} + \frac{\partial U^{x_2}}{\partial x_2} = 0$, where x_1, x_2, x_3 are permutations of x, y, z , $U^{x_1} = \int u^{x_1} dx_3$ and $U^{x_2} = \int u^{x_2} dx_3$. The resulting
 non-divergent flow field can then be expressed as a streamfunction ψ_3 defined by $\mathbf{U} = U^{x_1} \mathbf{x}_1 + U^{x_2} \mathbf{x}_2 = (-\nabla \times \psi_3 \mathbf{x}_3)$.

446 The depth-integrated circulation in our simulations stands in stark contrast to that of Stommel
 447 and Arons (1959a)'s barotropic model and is the expression of a combination of various baro-
 448 clinic deep western boundary currents and mixing layer flows (Figure 4b). Within 2000 km of
 449 the equator, the northward and southward components of the deep western boundary currents al-
 450 ternatively dominate (compare with the meridional velocity at the equator in Figure 3). North of
 451 $y = 2000$ km, the barotropic circulation is dominated by the along-slope flow in the bottom bound-
 452 ary layer, which is opposite the direction of Kelvin wave propagation. The barotropic circulation
 453 both near the boundaries and in the interior is strongly influenced by mixing layer dynamics and is
 454 structurally distinct from that predicted by the linear response to vortex stretching (Stommel and
 455 Arons 1959b; Pedlosky 1992; Cember 1998).

456 *c. Partially-Compensating Watermass Transformations*

457 The watermass transformation represents the net flow across a buoyancy surface driven by di-
 458 abatic forcing. Watermass transformation in the PGCM is driven by: bottom-enhanced turbulent
 459 mixing (positive in the net), restoring to a reference buoyancy profile in the southern restoring re-
 460 gion (negative in the net), and a negligible positive contribution from a background turbulent flux
 461 across the upper boundary. In the northern hemisphere, the restoring rate vanishes by construc-
 462 tion and watermass transformation is dominated by the mixing-driven component. Its calculation,
 463 following Walin (1982) and Ferrari et al. (2016), is given by

$$T(b) = \frac{\partial}{\partial b} \int_{V_{b' < b}} \nabla \cdot (\kappa \nabla b') dV, \quad (18)$$

464 where $V_{b' < b}$ is the volume of water less buoyant than b . Watermass transformation is conveniently
 465 expressed in units of volumetric transport (m^3/s) and can be decomposed into various contribu-
 466 tions. When applied to regions of bottom-enhanced mixing in the abyss, it is informative to de-

467 compose the net watermass transformation into the typically negative contribution (balanced by
 468 diapycnal downwelling) in the SML and the typically positive contribution (balanced by diapycnal
 469 upwelling) in the BBL (e.g. Ferrari et al. 2016; McDougall and Ferrari 2016). For the purposes of
 470 watermass transformation calculations in this paper, we define the BBL as the layer with a con-
 471 vergent buoyancy flux, $\nabla \cdot (\kappa \nabla b) > 0$, which extends upwards from the seafloor to the first zero
 472 crossing of the buoyancy flux divergence; the remainder of the ocean is considered the SML and is
 473 dominated by a buoyancy flux divergence, $\nabla \cdot (\kappa \nabla b) < 0$. For convenience, all watermass transfor-
 474 mations in this paper are computed in buoyancy space and remapped into depth space according
 475 to the average depth of buoyancy surfaces,

$$\bar{z} = \frac{1}{A(b)} \int z(b) dA, \quad (19)$$

476 which facilitates comparing across simulations with dramatically different stratifications and com-
 477 paring against the fixed depths of topographic features in the ocean.

478 The net northern hemisphere watermass transformation of $T_{\text{net}} = 1.6$ Sv at 3750 m (Figure 5a),
 479 where it reaches its maximum, is consistent with the depth and magnitude of the maximum of
 480 the MOC streamfunction at the equator (Figure 4a). The net watermass transformation $T_{\text{net}} =$
 481 $T_{\text{BBL}} + T_{\text{SML}} = 1.6$ Sv (black line) is the residual of a positive contribution of $T_{\text{BBL}} = 2.1$ Sv from
 482 the BBL (red line) and a negative contribution of $T_{\text{SML}} = -0.5$ Sv from the SML (blue line), both
 483 of which are dominated by the vertical component of the buoyancy flux divergence (dashed lines),
 484 i.e.

$$T(b) = \partial_b \int_{V_{b' < b}} \nabla \cdot (\kappa \nabla b') dV \simeq \partial_b \int_{V_{b' < b}} \partial_z (\kappa b'_z) dV. \quad (20)$$

485 Virtually all of this transformation occurs on the flanks of the mid-ocean ridge (Figure 5b).

486 For the convenience of being able to ignore meridional variations in the the basin geometry,
 487 we limit the remaining discussion to a domain from $L/2 < x < 3L/2$ and $0 < y < L/2$ along

488 the north-hemisphere mid-ocean ridge, which is responsible for roughly 1 Sv of the full basin's
 489 transformation (Figure 5c; limited domain outlined in Figure 12e).

490 The net watermass transformation $T_{\text{net}} = 1$ Sv at equilibrium is much larger than the $L\Psi_{\text{bg}} \leq$
 491 0.1 Sv predicted by the integral constraint (eq. 5) from 1D boundary layer theory. To clarify
 492 the discrepancy between the watermass transformations that emerge from the 3D PGCM and the
 493 watermass transformations predicted by 1D dynamics, we emulate the 3D PGCM simulation by
 494 solving the 1D boundary layer equations locally and interpolating onto the 3D PGCM grid.

495 5. Emulating the 3D PGCM with local 1D boundary layer models

496 a. Boundary layer theory

497 Following Callies and Ferrari (2018), we transform the planetary-geostrophic equations (6) - (8)
 498 from the Cartesian coordinates (x, y, z) to a coordinate system (x', y', z') aligned with an infinitely
 499 extending sea floor at $z = x \tan \theta$, with slope angle θ , and ignoring the restoring condition on
 500 buoyancy. The transformation is given by $x' = x \cos \theta + z \sin \theta$, $y' = y$, $z' = -x \sin \theta + z \cos \theta$.
 501 Buoyancy $b = B(z) + b'$ is decomposed into a background $B(z)$ with constant stratification $B_z = N_0^2$
 502 and an anomaly $b'(z')$. The boundary layer equations are thus given by:

$$-f \cos \theta u^{y'} = b' \sin \theta - r \cos \theta^2 u^{x'} \quad (21)$$

$$f \cos \theta u^{x'} = -r u^{y'} \quad (22)$$

$$b'_t + u^{x'} N_0^2 \sin \theta = \partial_{z'} [\kappa (N^2 \cos \theta + b'_{z'})], \quad (23)$$

503 with a no-flux boundary condition $b'_{z'} + N_0^2 \cos \theta = 0$ at the seafloor $z' = 0$ and decay conditions
 504 $u^{x'}, u^{y'}, b'_{z'} \rightarrow 0$ as $z' \rightarrow 0$. These equations yield exact analytical solutions for constant κ (Callies
 505 2018) and approximate analytical solutions for elementary structures of $\kappa(z)$ for certain steady
 506 state parameter regimes (Callies 2018).

507 *b. Emulator setup*

508 We emulate the PGCM solution by using finite differences to solve the time-dependent
509 boundary-layer equations (21) - (23) with the local Coriolis parameter $f(y)$ and slope angle $\theta(x,y)$
510 at each $(x,y) = (\xi, \eta)$ of the PGCM grid, which is a sensible approach given that the parameters
511 $f(y)$ and $\theta(x,y)$ vary on scales larger than the those of the boundary-layer solutions (Dell and Pratt
512 2015). Since these local boundary layer solutions are given in terms of the local slope-normal di-
513 rection z' rather than the true vertical direction z , we project the solution onto the true vertical
514 direction z with the substitution $z' \rightarrow z/\cos \theta$ and linearly interpolate from the projected boundary
515 layer finite differences z -levels to the PGCM's local σ -levels. This process provides an emulator
516 of the PGCM which is purely the result of local 1D dynamics but is re-gridded to the same grid as
517 the 3D PGCM and can thus be directly compared.

518 *c. Emulator evaluation*

519 We evaluate the emulator against the spin-up of a PGCM simulation with a constant stratification
520 initial condition N_0^2 , hereafter PGCM-CONST. The 1D emulator accurately reproduces the initial
521 spin-up of buoyancy and velocity fields of the PGCM-CONST simulation well along most of the
522 mid-ocean ridge flanks, but fails at the top and bottom of the ridge where the topographic curvature
523 is large and the cross-slope convergences omitted by 1D dynamics become important (Figure 6,
524 upper).

525 As the solution nears equilibrium, however, the interior basin stratification drifts away from its
526 constant initial value (compare gray and black contours in Figure 6d) and the boundary layer flows
527 diverge quantitatively from the 1D emulator's prediction (Figure 6c,d). This is expected, as the
528 basin stratification of PGCM-CONST is allowed to evolve in response to the 3D circulation while
529 the background interior stratification N_0^2 is a constant parameter in the 1D boundary layer models

530 that populate the emulator. Relative to the emulator, the equilibrium PGCM-CONST solution
531 exhibits reduced downwelling in the SML and enhanced upwelling in the BBL, both of which
532 contribute to enhancing the net diapycnal upwelling. In Section 6, we use the 1D emulator in the
533 context of watermass transformations to identify properties of the watermass transformations in
534 the PGCM that can be explained by one-dimensional dynamics alone.

535 **6. The Effect of Variable Interior Stratification on the Abyssal Circulation**

536 *a. What sets the abyssal stratification?*

537 In our PGCM simulations, the drift of interior buoyancy surfaces over time (Figure 6d) suggests
538 that the interior stratification at equilibrium may differ substantially from the stratification of the
539 reference buoyancy profile. Figure 7 shows the temporal evolution of the horizontally-averaged
540 vertical stratification profile, averaged over the northern hemisphere basin in the PGCM, where
541 darker greys represent later times. In simulations with constant stratification reference buoyancy
542 profiles, the abyssal stratification develops substantial vertical structure in the basin over time,
543 despite being rapidly restored back to a constant stratification in the southern restoring region
544 (solid lines, Figure 7a). The details of the vertical structure of the equilibrium basin stratification
545 depend on ridge height (compare Figure 7a,b), but in either case the basin stratification increases
546 from zero at the maximum depth (imposed by the no-flux condition at the flat bottom) up to near
547 the restoring reference value at the top boundary.

548 Simulations using a reference buoyancy profile that corresponds to an exponential stratification
549 with decay scale of $\delta = 1000$ m exhibit much less drift in their stratifications over time (dashed
550 lines, Figure 7a,b). Although the equilibrium basin stratifications in all of the different PGCM
551 experiments develop vertical structure, there does not seem to be a single preferred equilibrium

552 stratification that depends only on the mixing: both the geometry of the abyssal topography and
553 the boundary conditions in the southern restoring region influence the interior stratification at
554 equilibrium.

555 *b. Effect of variable stratification on watermass transformations*

556 We begin by considering the case of transient spin-up from a reference buoyancy profile with
557 constant stratification N_0^2 , PGCM-CONST. It is useful to consider the evolution of the PGCM dur-
558 ing its initial spin-up (i.e. near $\hat{t} \simeq \tau_{\text{BL}}/\tau = 0.1$) when only mixing layer dynamics are relevant
559 and the solution is thus well-predicted by the 1D Emulator (Figure 6). Figure 8a shows the water-
560 mass transformations in the 1D Emulator at $\hat{t} = 0.1$, which almost exactly predicts the watermass
561 transformations in the full 3D PGCM (Figure 8b).

562 Between $-4200 \text{ m} < z < -3000 \text{ m}$, where the slope of the mid-ocean ridge is roughly constant,
563 the near-boundary flow exhibits a vanishingly small net transport (solid black line in Figure 8a),
564 which is approximately equal to the integral constraint $T_{\text{net}} \simeq L\Psi_{\text{bg}} = L\kappa_{\text{bg}} \cot \theta \leq 0.1 \text{ Sv}$ predicted
565 by 1D boundary layer theory (dashed black line in Figure 8a). This vanishingly small net transport
566 is the result of large positive transformation T_{BBL} (diabatic upwelling, in red) in the BBL and
567 almost-as-large negative transformation T_{SML} (diabatic downwelling, in blue) in the SML. Below
568 $z = -4200 \text{ m}$, at the base of the topographic slope, abyssal bottom waters feed the upwelling in the
569 BBL and the maximum net watermass transformation is well predicted by the strictly upwelling
570 transport in the bottom boundary layer from 1D theory (Figure 8a,b), as suggested by Callies and
571 Ferrari (2018).

572 For the spin-up from a reference stratification that increases exponentially with height (as is al-
573 most ubiquitously the case in the abyssal ocean), the integral constraint (eq. 5) no longer holds at
574 $\hat{t} = 0.1$ and the solution already exhibits a net transformation much larger than $L\Psi_{\text{bg}}$ at all depths

575 from the base of the slope to the ridge crest (Figure 8c,d). The increase in the net transformation,
 576 which spans the full vertical extent of the ridge, is primarily due to a decrease in the downwelling
 577 in the SML which, in the extreme case of an exponential scale height of $\delta = 500$ m for the stratifi-
 578 cation, vanishes completely (Figure 8d). The strongly positive net transformation is largely due to
 579 the buoyancy convergence driven by the rapid increase of the initial stratification with height, i.e.
 580 $\nabla \cdot (\kappa \nabla b) \simeq \partial_z(\kappa B_z) \sim \kappa B_{zz} > 0$.

581 As these solutions reach equilibrium, they retain a finite net transformation at all depths from the
 582 base of the slope to the ridge crest, slightly reduced by gradually strengthening negative transfor-
 583 mations in the SML (compare Figure 8g,h to Figure 8c,d). At equilibrium, we find the degree of
 584 compensation near the ridge crest depends strongly on the vertical scale over which the restoring
 585 stratification varies (within a range applicable to the ocean): the more rapidly the stratification
 586 increases with height, the less upwelling in the BBL is compensated by downwelling in the SML
 587 (Figure 8f-h and Figure 9). In contrast, upwelling in the BBL is remarkably invariant to vertical
 588 variations in the stratification and remains a reasonable prediction for the maximum net transfor-
 589 mation (Figure 9), which occurs at the base of the slope where the compensating downwelling
 590 contribution from the SML vanishes (Figure 9c). Thus, while the maximum net watermass trans-
 591 formation is accurately predicted by upwelling in the BBL alone, the vertical structure and extent
 592 of watermass transformations depend equally on downwelling in the SML, which itself is strongly
 593 dependent on the vertical stratification.

594 The integral constraint from 1D theory does not hold at any depth in any of the PGCM solutions,
 595 including PGCM-CONST, in which a constant stratification is continuously being restored in the
 596 southern restoring region (Figure 8f). We attribute this to the fact that even when the stratification
 597 is held roughly constant in the southern restoring region, the interior stratification in the rest of the

598 basin drifts significantly away from the reference profile, as discussed in Section 6a and shown in
599 Figure 7.

600 *c. Vertical extent of overturning set by ridge height*

601 Since we have shown that most of the watermass transformation occurs within bottom mixing
602 layers along the mid-ocean ridge (Figure 5a,b), we further hypothesize that variations in the height
603 of the ridge modulate the vertical extent of abyssal watermass transformations and thus the vertical
604 extent of the abyssal overturning cell. We test this hypothesis by running variations of the PGCM-
605 CONST where we vary the ridge height from 500 m to 2000 m, in increments of 500 m. In the
606 initial spin-up, largely compensating positive and negative transformations develop in the BBL
607 and SML, respectively, from the base of the ridge slope up to the ridge crest (Figure 10a-d). The
608 net transformation below the ridge crest vanishes according to the integral constraint (eq. 5),
609 except near the sea-floor where bottom water feeds into the BBL. At equilibrium, however, the
610 stratification drifts away from its constant reference state (e.g. Figure 7) and permits a finite net
611 transformation (Figure 10e-h), which spans the full vertical extent of the ridge. The result that the
612 vertical extent of the abyssal MOC follows the vertical extent of the mid-ocean ridge is consistent
613 with Lumpkin and Speer (2007)'s global inversion for the MOC, which shows that the vertical
614 extent of the Atlantic and Indo-Pacific MOCs appear to closely follow the vertical extent of their
615 respective major bathymetric features (i.e. mid-ocean ridges).

616 **7. Comparison with realistic mid-ocean ridges**

617 The topography and mixing in the PGCM is inspired by observations from the Brazil Basin (Fig-
618 ure 11), one of the regions of the abyssal ocean best characterized by observations (e.g. St. Laurent
619 et al. 2001; Thurnherr and Speer 2003). The circulation that emerges from the PGCM-REAL sim-

620 ulation (Figure 11b) is qualitatively similar to the circulation inferred from observations using an
621 inverse model (Figure 11a, based on St. Laurent et al. 2001): bottom-enhanced mixing along the
622 slope of the mid-ocean ridge drives upwelling in a bottom boundary layer and downwelling in a
623 stratified mixing layer above.

624 We estimate watermass transformations in the ocean following Ferrari et al. (2016)’s modifica-
625 tions of Nikurashin and Ferrari (2013). The buoyancy flux is parameterized by $\overline{w'b'} = -\Gamma\varepsilon$, with
626 the commonly-used constant value $\Gamma = 0.2$ for the ‘mixing efficiency’ (Osborn 1980); the buoy-
627 ancy field is taken from a gridded product derived from hydrographic sections of the World Ocean
628 Circulation Experiment (Gouretski and Koltermann 2004); and we impose the no-flux bottom
629 boundary condition $\mathbf{n} \cdot \overline{\mathbf{u}'b'} \simeq \overline{w'b'} = 0$ (where $\mathbf{n} \simeq \mathbf{z}$ for typical bathymetric slopes of $\tan \theta \ll 1$)
630 by making the buoyancy flux go to zero linearly in the bottom grid cell of each grid column, which
631 are nominally 250 m thick. The dissipation rate ε is produced by applying linear wave radiation
632 theory for internal tides (Nycander 2005) and lee waves (Nikurashin and Ferrari 2011) and assum-
633 ing a fraction $q = 0.3$ of the radiated energy is locally dissipated according to a bottom-enhanced
634 structure function with a height scale of 500 m (St. Laurent and Garrett 2002). We compare wa-
635 termass transformation estimates from the ocean with estimates from PGCM-REAL, a simulation
636 with restoring to an exponential reference stratification with a decay scale of 1000 m and which
637 is our simulation with a stratification in the southern restoring region most similar to the South-
638 ern Ocean’s (Figure 2c). We focus on rectangular regions with dimensions 3000 km by 3000 km
639 (in the PGCM) or 30° longitude by 30° latitude (in the ocean), which encompass comparable
640 ridge lengths and surface areas at subtropical latitudes. Watermass transformations in the PGCM-
641 REAL simulation (Figure 12a) are the result of partially compensating buoyancy flux convergence
642 (Figure 12e) in the BBL (red colors) and buoyancy flux divergence in the SML (blue colors).
643 Qualitatively similar (but noisier) watermass transformations emerge for the mid-ocean ridge re-

644 gions in the Pacific, Atlantic, and Indian (Figure 12b-d, regions delineated by boxes in panels e,f).
645 This remarkable similarity emerges in the large-scale watermass diagnostic despite the extremely
646 heterogeneous nature of the estimated buoyancy flux and topography in the ocean basins (Figure
647 12f), relative to the smoothly varying nature of our idealized model (Figure 12e). Estimates of
648 *global* abyssal watermass transformations, however, exhibit relatively stronger compensation by
649 downwelling in the SML than shown here for mid-ocean ridge regions (Ferrari et al. 2016).

650 8. Classic recipes and new trends in abyssal cuisine

651 Quantitative study of the abyssal stratification begins with the classic study of Munk (1966): a
652 point-wise theory in which the observed abyssal stratification is the result of a balance between
653 uniform upwelling and a uniform turbulent vertical mixing. As anticipated by Munk (1966), sub-
654 sequent observations show turbulent mixing to be strongly heterogeneous, with an emerging pat-
655 tern of weak background mixing and vigorous mixing near rough topography (Polzin et al. 1997;
656 Waterhouse et al. 2014). In light of these observations, Munk and Wunsch (1998) revisit Munk
657 (1966)’s theorized point-wise vertical balance and re-derive it as a horizontally-averaged buoyancy
658 budget, which we transcribe as

$$\langle w \rangle A \simeq \frac{A(z)}{\langle N^2 \rangle} \frac{d}{dz} [\langle \kappa \rangle \langle N^2 \rangle] \quad (24)$$

659 in our notation, where the key assumption is that correlations between the turbulent diffusivity
660 κ , the stratification N^2 , and the vertical velocity w are all assumed to be negligible, such that
661 $\langle wN^2 \rangle = \langle w \rangle \langle N^2 \rangle$ and $\langle \kappa N^2 \rangle = \langle \kappa \rangle \langle N^2 \rangle$. In Figure 13 (blue lines), we show, respectively, the
662 horizontally-averaged stratification $\langle N^2 \rangle$ and turbulent diffusivity $\langle \kappa \rangle$, the isobath surface area
663 (ocean area at a fixed depth) $A(z)$, and the upwelling transport $\langle w \rangle A$ predicted by equation 24 in
664 three different PGCM experiments at equilibrium. The horizontally-averaged vertical flux diver-

665 gence (eq. 24) is a poor prediction for the diagnosed vertical transport in all three cases, even if
666 the point-wise balance still holds throughout. This is not surprising, given that w , N^2 , and κ co-
667 vary in our solutions and that density surfaces are strongly sloping near boundaries, so analysis in
668 buoyancy coordinates (such as watermass transformation analysis) which accounts for these cor-
669 relations is more appropriate. In contrast, the upwelling transport predicted by the mixing-driven
670 watermass transformation (solid black line, where it has been remapped into depth coordinates)
671 compares favorably with the diagnosed upwelling transport (dashed black line) in Figure 13. As
672 observations and theories of spatially-heterogeneous turbulent mixing become more complete, the
673 watermass transformation framework is likely to become an increasingly promising tool for esti-
674 mating and understanding abyssal upwelling.

675 **9. Discussion**

676 The idealized numerical model presented here describes an abyssal circulation and stratification
677 controlled by mixing-driven flows along a mid-ocean ridge in a cross-equatorial basin (Figure
678 1). By initializing with- and restoring to- a series of reference buoyancy profiles in the south of
679 the basin, we investigate transient and equilibrium coupling between the basin stratification and
680 the mixing-driven boundary flows. At equilibrium, abyssal waters form in the southern restoring
681 region and flow north via adiabatic deep western boundary currents (red circle), filling the abyssal
682 depths in both hemispheres. Along the mid-ocean ridge, bottom-enhanced mixing (squiggly lines)
683 drives a net transformation of dense abyssal waters into lighter deep waters (dashed arrows), the
684 residual of partially-compensating upwelling in a bottom boundary layer (BBL) and downwelling
685 in a stratified mixing layer (SML) right above it. The newly formed deep waters flow zonally
686 towards the western continental slope (solid arrow), returning southward via an adiabatic deep

687 western boundary current to the restoring region (blue circles), and closing the abyssal overturning
688 circulation as they are once again transformed into dense bottom waters.

689 Despite the extreme degree of idealization in our formulation of the PGCM, the watermass
690 transformations that emerge at equilibrium are qualitatively similar to diagnostic estimates of wa-
691 termass transformations near mid-ocean ridges in the Pacific, Atlantic, and Indian Oceans (Figure
692 12), which are themselves fairly uncertain (Cimoli et al. 2019). Similarly, the zonal overturn-
693 ing that emerges within bottom mixing-driven flows along the mid-ocean ridge are qualitatively
694 similar to that described by an inverse model of the abyssal Brazil Basin (St. Laurent et al. 2001).

695 The equilibrium interior stratification in the PGCM always exhibits dynamically significant ver-
696 tical variations, the structure of which is determined by a combination of mixing layer dynamics
697 and the restoring condition in the south. Even in our PGCM-CONST simulations that are ini-
698 tialized from and restored to a constant stratification reference buoyancy profile, heterogeneities
699 in the topographic slope cause cross-slope diverges and a corresponding exchange flow between
700 the bottom mixing layers and the interior. Over time, these exchange flows modify the interior
701 stratification and associated watermass transformations.

702 As in Callies and Ferrari (2018), we find the prediction of upwelling in the BBL by one-
703 dimensional (1D) boundary layer theory provides a reasonable approximation to the maximum
704 net transformation or, equivalently, the strength of the diabatic meridional overturning circulation
705 (Figures 8 and 9). While this interpretation provides a useful prediction for the maximum net
706 transformation which occurs at the base of topographic slopes, it does not inform the net transfor-
707 mation along the flanks of the mid-ocean ridge, where upwelling in the BBL is instead partially
708 compensated by downwelling in a SML. At depths where both the BBL and the SML are ac-
709 tive, 1D theory predicts almost perfect compensation and a resulting net transformation that is
710 vanishingly small (eq. 5 and Figure 8a,e). In contrast, our PGCM simulations exhibit finite net

711 watermass transformations that extend from the base of the ridge slopes all the way up to the ridge
712 crest (Figure 10), consistent with both our oceanic estimates (Figure 12) and inverse models of the
713 Indo-Pacific overturning circulation (Lumpkin and Speer 2007). We attribute the existence of a
714 finite net transformation to vertical variations in the basin stratification (Figure 8). As we increase
715 the degree to which the restoring stratification varies in the vertical, the compensation of BBL
716 upwelling by SML downwelling (evaluated near the depth of the ridge crest) ranges from nearly-
717 perfect compensation to nearly-zero compensation (Figure 9a). Thus, while 1D bottom boundary
718 layer theory provides a reasonable approximation to *maximum net* watermass transformation, the
719 vertical extent and structure of watermass transformations depends on the degree of compensation
720 by downwelling in the SML, which is itself coupled to the vertically-varying basin stratification.

721 Despite our improved understanding of the roles of bottom mixing and the interior basin strat-
722 ification on the abyssal watermass transformations and circulation, we fall short of a predictive
723 analytical theory for the abyssal overturning and stratification that couples boundary layer dynam-
724 ics with a model for the evolution of the interior stratification.

725 *Acknowledgments.* We thank Ali Mashayek, Laura Cimoli, Xiaozhou Ruan, and Bryan Kaiser
726 for insightful discussions about bottom mixing layers. We thank Ali Mashayek for sharing three-
727 dimensional maps of the turbulent vertical buoyancy flux from Nikurashin and Ferrari (2013) and
728 Ferrari et al. (2016), which we use in Section 7.

729 APPENDIX

730 The planetary-geostrophic equations (6) - (8) are solved numerically in non-dimensional terrain-
731 following coordinates (e.g. Salmon 1998)

$$\hat{\xi} = \frac{x}{L}, \quad \hat{\eta} = \frac{y}{L}, \quad \hat{\sigma} = \frac{z}{d(x,y)} \quad (\text{A1})$$

732 (see Callies and Ferrari 2018 and their Appendix B for details). The cost of transforming to terrain-
 733 following coordinates is the appearance of cross terms in the diffusion operator, but the additional
 734 terms are manageable when the equations are written in tensor calculus notation (e.g. Grinfeld
 735 2013). The benefit of terrain-following coordinates is that the bottom boundary conditions $\mathbf{n} \cdot \mathbf{u} = 0$
 736 and $\mathbf{n} \cdot \nabla b$ at $z = -d(x, y)$ become simply $\hat{u}^{\hat{\sigma}} = 0$ and $\nabla^{\hat{\sigma}} \hat{b} = 0$ at $\hat{\sigma} = -1$, where upper indices
 737 denote contravariant components. The terrain-following coordinates allow the depth $d(x, y)$ to
 738 smoothly taper to zero at the domain boundaries, avoiding the need for unrealistic non-hydrostatic
 739 upwelling layers at the vertical sidewalls (Salmon 1992), and instead allowing thin near-boundary
 740 flows along sloping boundaries such as the bottom mixing layers (Callies and Ferrari 2018). The
 741 resulting boundary layers agree well with predictions from one-dimensional boundary theory, even
 742 at relatively coarse “vertical” $\hat{\sigma}$ -resolution (Callies and Ferrari 2018; see also Figure 6).

743 The planetary-geostrophic system of equations (6) - (8) consists of a prognostic equation for
 744 buoyancy and diagnostic equations for momentum. We implement the dynamics by diagnosing
 745 the flow \mathbf{u} from the buoyancy b and using the diagnosed flow to step the buoyancy b forward in
 746 time. The inversion for the flow \mathbf{u} consists of three steps: first, we solve a two-dimensional elliptic
 747 problem for the barotropic, i.e. vertically-integrated, horizontal flow; second, we diagnose the
 748 baroclinic, i.e. vertically-varying, component of the horizontal flow from the frictionally modified
 749 thermal wind balance; third, we add the baroclinic and barotropic components of the horizontal
 750 flow and diagnose the vertical flow from the continuity equation. The details of this process and
 751 its derivation in terrain-following coordinates are provided in Appendix B of Callies and Ferrari
 752 (2018).

753 The equations are discretized using centered finite differences with fixed grid spacing of
 754 $\Delta \hat{\xi} = \Delta \hat{\eta} = 0.01$ and $\Delta \hat{\sigma} = 0.05$. Near the boundaries where centered finite differences is not
 755 possible, we use one-sided second-order differences for cross terms of the diffusive fluxes. The

756 grid is staggered such that buoyancy b and the barotropic streamfunction ψ are on cell centers and
757 the components of the velocity vector \mathbf{u} are on cell faces. Time-stepping with $\Delta t = 2.5 \times 10^{-5}$ is
758 explicit for advection, horizontal diffusion, and cross-terms in the vertical diffusion. We treat ver-
759 tical diffusion (excluding cross terms) implicitly because vertical grid spacing becomes very fine
760 near where the depth goes to zero and would require a prohibitively small timestep for numerical
761 stability.

762 **References**

- 763 Abernathey, R., D. Ferreira, and A. Klocker, 2013: Diagnostics of isopycnal mixing in a cir-
764 cumpolar channel. *Ocean Modelling*, **72**, 1–16, doi:10.1016/j.ocemod.2013.07.004, URL [http://](http://www.sciencedirect.com/science/article/pii/S1463500313001200)
765 www.sciencedirect.com/science/article/pii/S1463500313001200.
- 766 Abernathey, R. P., I. Cerovecki, P. R. Holland, E. Newsom, M. Mazloff, and L. D. Talley, 2016:
767 Water-mass transformation by sea ice in the upper branch of the Southern Ocean overturn-
768 ing. *Nature Geoscience*, **9** (8), 596–601, doi:10.1038/ngeo2749, URL [http://www.nature.com/](http://www.nature.com/articles/ngeo2749)
769 [articles/ngeo2749](http://www.nature.com/articles/ngeo2749), publisher: Nature Publishing Group.
- 770 Archer, D., H. Kheshgi, and E. Maier-Reimer, 1998: Dynamics of fossil fuel CO₂ neutralization
771 by marine CaCO₃. *Global Biogeochemical Cycles*, **12** (2), 259–276, doi:10.1029/98GB00744,
772 URL <http://doi.wiley.com/10.1029/98GB00744>.
- 773 Bezanson, J., A. Edelman, S. Karpinski, and V. Shah, 2017: Julia: A Fresh Approach to Numerical
774 Computing. *SIAM Review*, **59** (1), 65–98, doi:10.1137/141000671, URL [https://epubs.siam.org/](https://epubs.siam.org/doi/10.1137/141000671)
775 [doi/10.1137/141000671](https://epubs.siam.org/doi/10.1137/141000671).
- 776 Bryan, K., and L. J. Lewis, 1979: A water mass model of the world ocean. *Journal of Geophysical*
777 *Research*, **84** (C5), 2503–2517, doi:10.1029/JC084iC05p02503, iSBN: 0148-0227.

- 778 Callies, J., 2018: Restratification of Abyssal Mixing Layers by Submesoscale Baroclinic Eddies.
779 *Journal of Physical Oceanography*, JPO–D–18–0082.1, doi:10.1175/JPO-D-18-0082.1, URL
780 <http://journals.ametsoc.org/doi/10.1175/JPO-D-18-0082.1>.
- 781 Callies, J., and R. Ferrari, 2018: Dynamics of an Abyssal Circulation Driven by Bottom-
782 Intensified Mixing on Slopes. *Journal of Physical Oceanography*, **48** (6), 1257–1282, doi:
783 10.1175/JPO-D-17-0125.1, URL <http://journals.ametsoc.org/doi/10.1175/JPO-D-17-0125.1>.
- 784 Cember, R. P., 1998: On deep western boundary currents. *Journal of Geophysical Research:*
785 *Oceans*, **103** (C3), 5397–5417, doi:10.1029/97JC02422, URL <https://agupubs.onlinelibrary.wiley.com/doi/abs/10.1029/97JC02422>.
- 787 Cimoli, L., C.-c. P. Caulfield, H. L. Johnson, D. P. Marshall, A. Mashayek, A. C. N. Garabato,
788 and C. Vic, 2019: Sensitivity of deep ocean mixing to local internal tide breaking and mixing
789 efficiency. *Geophysical Research Letters*, **n/a** (n/a), doi:10.1029/2019GL085056, URL <https://agupubs.onlinelibrary.wiley.com/doi/abs/10.1029/2019GL085056>.
- 791 de Lavergne, C., G. Madec, J. Le Sommer, A. J. G. Nurser, and A. C. Naveira Garabato, 2016:
792 The Impact of a Variable Mixing Efficiency on the Abyssal Overturning. *Journal of Physical*
793 *Oceanography*, **46** (2), 663–681, doi:10.1175/JPO-D-14-0259.1, URL <http://journals.ametsoc.org/doi/10.1175/JPO-D-14-0259.1>.
- 795 Dell, R., and L. Pratt, 2015: Diffusive boundary layers over varying topography. *Journal of Fluid*
796 *Mechanics*, **769**, 635–653, doi:10.1017/jfm.2015.88, URL http://www.journals.cambridge.org/abstract_S0022112015000889.
- 798 Emile-Geay, J., and G. Madec, 2009: Geothermal heating, diapycnal mixing and the abyssal circu-
799 lation. *Ocean Science*, **5** (2), 203–217, doi:10.5194/os-5-203-2009, URL <http://www.ocean-sci>.

800 net/5/203/2009/.

801 Ferrari, R., A. Mashayek, T. J. McDougall, M. Nikurashin, and J.-M. Campin, 2016: Turning
802 Ocean Mixing Upside Down. *Journal of Physical Oceanography*, **46** (7), 2239–2261, doi:10.
803 1175/JPO-D-15-0244.1, URL <http://journals.ametsoc.org/doi/10.1175/JPO-D-15-0244.1>.

804 Garrett, C., 1990: The role of secondary circulation in boundary mixing. *Journal of Geophysical*
805 *Research*, **95** (C3), 3181, doi:10.1029/JC095iC03p03181, URL <http://doi.wiley.com/10.1029/JC095iC03p03181>, publisher: Wiley-Blackwell.

807 Garrett, C., P. MacCready, and P. Rhines, 1993: Boundary Mixing and Arrested Ekman Layers:
808 Rotating Stratified Flow Near a Sloping Boundary. *Annual Review of Fluid Mechanics*, **25** (1),
809 291–323, doi:10.1146/annurev.fl.25.010193.001451, URL <http://www.annualreviews.org/doi/10.1146/annurev.fl.25.010193.001451>, publisher: Annual Reviews 4139 El Camino Way, P.O.
810 Box 10139, Palo Alto, CA 94303-0139, USA.

812 Gent, P. R., and J. C. McWilliams, 1990: Isopycnal Mixing in Ocean Circulation Models.
813 *Journal of Physical Oceanography*, **20** (1), 150–155, doi:10.1175/1520-0485(1990)020<0150:
814 IMIOCM>2.0.CO;2, URL [http://journals.ametsoc.org/doi/abs/10.1175/1520-0485\(1990\)020%3C0150:IMIOCM%3E2.0.CO;2](http://journals.ametsoc.org/doi/abs/10.1175/1520-0485(1990)020%3C0150:IMIOCM%3E2.0.CO;2), iISBN: 0022-3670.

816 Gouretski, V., and K. P. Koltermann, 2004: WOCE global hydrographic climatology. *Berichte des*
817 *BSH*, **35**, 1–52.

818 Greatbatch, R. J., and K. G. Lamb, 1990: On Parameterizing Vertical Mixing of Momentum in
819 Non-eddy Resolving Ocean Models. *Journal of Physical Oceanography*, **20** (10), 1634–1637,
820 doi:10.1175/1520-0485(1990)020<1634:OPVMOM>2.0.CO;2, URL <https://journals.ametsoc.org/doi/abs/10.1175/1520-0485%281990%29020%3C1634%3AOPVMOM%3E2.0.CO%3B2>.

- 822 Gregg, M. C., 1989: Scaling turbulent dissipation in the thermocline. *Journal of Geophysical*
823 *Research*, **94** (C7), 9686, doi:10.1029/JC094iC07p09686, URL [http://doi.wiley.com/10.1029/](http://doi.wiley.com/10.1029/JC094iC07p09686)
824 [JC094iC07p09686](http://doi.wiley.com/10.1029/JC094iC07p09686).
- 825 Grinfeld, P., 2013: *Introduction to Tensor Analysis and the Calculus of Moving Surfaces*. Springer-
826 Verlag, New York, URL <https://www.springer.com/gp/book/9781461478669>.
- 827 Hansen, J., G. Russell, A. Lacis, I. Fung, D. Rind, and P. Stone, 1985: Climate Response Times:
828 Dependence on Climate Sensitivity and Ocean Mixing. *Science*, **229** (4716), 857–859, doi:
829 [10.1126/science.229.4716.857](http://www.sciencemag.org/cgi/doi/10.1126/science.229.4716.857), URL [http://www.sciencemag.org/cgi/doi/10.1126/science.229.](http://www.sciencemag.org/cgi/doi/10.1126/science.229.4716.857)
830 [4716.857](http://www.sciencemag.org/cgi/doi/10.1126/science.229.4716.857).
- 831 Holden, P. B., N. R. Edwards, K. Fraedrich, E. Kirk, F. Lunkeit, and X. Zhu, 2016:
832 PLASIMGENIE v1.0: a new intermediate complexity AOGCM. *Geoscientific Model Devel-*
833 *opment*, **9** (9), 3347–3361, doi:<https://doi.org/10.5194/gmd-9-3347-2016>, URL [https://www.](https://www.geosci-model-dev.net/9/3347/2016/)
834 [geosci-model-dev.net/9/3347/2016/](https://www.geosci-model-dev.net/9/3347/2016/).
- 835 Holmes, R. M., C. de Lavergne, and T. J. McDougall, 2018: Ridges, Seamounts, Troughs, and
836 Bowls: Topographic Control of the Diapycnal Circulation in the Abyssal Ocean. *Journal of*
837 *Physical Oceanography*, **48** (4), 861–882, doi:10.1175/JPO-D-17-0141.1, URL [http://journals.](http://journals.ametsoc.org/doi/10.1175/JPO-D-17-0141.1)
838 [ametsoc.org/doi/10.1175/JPO-D-17-0141.1](http://journals.ametsoc.org/doi/10.1175/JPO-D-17-0141.1).
- 839 Huang, R. X., and X. Jin, 2002: Deep Circulation in the South Atlantic Induced by Bottom-
840 Intensified Mixing over the Mid-ocean Ridge*. *Journal of Physical Oceanography*, **32** (4), 1150–
841 1164, doi:10.1175/1520-0485(2002)032<1150:DCITSA>2.0.CO;2.
- 842 Jayne, S. R., 2009: The Impact of Abyssal Mixing Parameterizations in an Ocean General Circula-
843 tion Model. *Journal of Physical Oceanography*, **39** (7), 1756–1775, doi:10.1175/2009JPO4085.

844 1.

845 Kawase, M., 1987: Establishment of Deep Ocean Circulation Driven by Deep-Water Produc-
846 tion. *Journal of Physical Oceanography*, **17** (12), 2294–2317, doi:10.1175/1520-0485(1987)
847 017(2294:EODOCD)2.0.CO;2.

848 Koltermann, K. P., V. Gouretski, and K. Jancke, 2011: *Hydrographic Atlas of the World Ocean*
849 *Circulation Experiment (WOCE): Volume 3: Atlantic Ocean*. National Oceanography Centre.

850 Ledwell, J. R., E. T. Montgomery, K. L. Polzin, L. C. St. Laurent, R. W. Schmitt, and J. M.
851 Toole, 2000: Evidence for enhanced mixing over rough topography in the abyssal ocean. *Nature*,
852 **403** (6766), 179–182, doi:10.1038/35003164, URL <http://www.nature.com/articles/35003164>,
853 publisher: Nature Publishing Group.

854 Ledwell, J. R., A. J. Watson, and C. S. Law, 1993: Evidence for slow mixing across the py-
855 cnocline from an open-ocean tracer-release experiment. *Nature*, **364** (6439), 701–703, doi:
856 10.1038/364701a0, URL <http://www.nature.com/doi/10.1038/364701a0>, publisher: Na-
857 ture Publishing Group.

858 Lumpkin, R., and K. Speer, 2007: Global Ocean Meridional Overturning. *Journal of Physical*
859 *Oceanography*, **37** (10), 2550–2562, doi:10.1175/JPO3130.1, URL [http://dx.doi.org/10.1175/](http://dx.doi.org/10.1175/JPO3130.1)
860 [JPO3130.1](http://dx.doi.org/10.1175/JPO3130.1), iISBN: 0022-3670.

861 Marotzke, J., 1997: Boundary Mixing and the Dynamics of Three-Dimensional Thermo-
862 haline Circulations. *Journal of Physical Oceanography*, **27** (8), 1713–1728, doi:10.1175/
863 1520-0485(1997)027(1713:BMATDO)2.0.CO;2, URL [https://journals.ametsoc.org/doi/full/10.](https://journals.ametsoc.org/doi/full/10.1175/1520-0485%281997%29027%3C1713%3ABMATDO%3E2.0.CO%3B2)
864 [1175/1520-0485%281997%29027%3C1713%3ABMATDO%3E2.0.CO%3B2](https://journals.ametsoc.org/doi/full/10.1175/1520-0485%281997%29027%3C1713%3ABMATDO%3E2.0.CO%3B2).

865 Marshall, J., and T. Radko, 2003: Residual-Mean Solutions for the Antarctic Circumpolar Current
866 and Its Associated Overturning Circulation. *Journal of Physical Oceanography*, **33** (11), 2341–
867 2354, doi:10.1175/1520-0485(2003)033<2341:RSFTAC>2.0.CO;2, URL [http://dx.doi.org/10.1175/1520-0485\(2003\)033%3C2341:RSFTAC%3E2.0.CO;2](http://dx.doi.org/10.1175/1520-0485(2003)033%3C2341:RSFTAC%3E2.0.CO;2), iSBN: 0022-3670.

869 Marshall, J., and K. Speer, 2012: Closure of the meridional overturning circulation through
870 Southern Ocean upwelling. *Nature Geoscience*, **5** (3), 171–180, doi:10.1038/ngeo1391, URL
871 <http://dx.doi.org/10.1038/ngeo1391>, publisher: Nature Publishing Group iSBN: 1752-0894.

872 McDougall, T. J., and R. Ferrari, 2016: Abyssal Upwelling and Downwelling Driven by
873 Near-Boundary Mixing. *Journal of Physical Oceanography*, **47** (2), 261–283, doi:10.1175/
874 JPO-D-16-0082.1, URL <https://journals.ametsoc.org/doi/full/10.1175/JPO-D-16-0082.1>.

875 Melet, A., S. Legg, and R. Hallberg, 2016: Climatic Impacts of Parameterized Local and Remote
876 Tidal Mixing. *Journal of Climate*, **29** (10), 3473–3500, doi:10.1175/JCLI-D-15-0153.1, URL
877 <http://journals.ametsoc.org/doi/10.1175/JCLI-D-15-0153.1>.

878 Munk, W. H., 1966: Abyssal recipes. *Deep Sea Research and Oceanographic Abstracts*, **13** (4),
879 707–730, doi:10.1016/0011-7471(66)90602-4, arXiv: cs/9605103 iSBN: 1600117471.

880 Munk, W. H., and C. Wunsch, 1998: Abyssal Recipes II: energetics of tidal and wind mixing.
881 *Deep-Sea Research Part I: Oceanographic Research Papers*, **45**, 1978–2010.

882 Nikurashin, M., and R. Ferrari, 2009: Radiation and Dissipation of Internal Waves Generated
883 by Geostrophic Motions Impinging on Small-Scale Topography: Theory. *Journal of Phys-
884 ical Oceanography*, **40** (5), 1055–1074, doi:10.1175/2009JPO4199.1, URL [https://journals.
885 ametsoc.org/doi/full/10.1175/2009JPO4199.1](https://journals.ametsoc.org/doi/full/10.1175/2009JPO4199.1).

- 886 Nikurashin, M., and R. Ferrari, 2011: Global energy conversion rate from geostrophic
887 flows into internal lee waves in the deep ocean. *Geophysical Research Letters*, **38** (8),
888 doi:10.1029/2011GL046576, URL [https://agupubs.onlinelibrary.wiley.com/doi/abs/10.1029/
889 2011GL046576](https://agupubs.onlinelibrary.wiley.com/doi/abs/10.1029/2011GL046576).
- 890 Nikurashin, M., and R. Ferrari, 2013: Overturning circulation driven by breaking internal waves
891 in the deep ocean. *Geophysical Research Letters*, **40** (12), 3133–3137, doi:10.1002/grl.50542,
892 URL <http://doi.wiley.com/10.1002/grl.50542>, publisher: Wiley-Blackwell.
- 893 Nikurashin, M., and S. Legg, 2011: A Mechanism for Local Dissipation of Internal Tides
894 Generated at Rough Topography. *Journal of Physical Oceanography*, **41** (2), 378–395, doi:
895 10.1175/2010JPO4522.1, URL <http://journals.ametsoc.org/doi/abs/10.1175/2010JPO4522.1>.
- 896 Nikurashin, M., and G. Vallis, 2011: A Theory of Deep Stratification and Overturning Circulation
897 in the Ocean. *Journal of Physical Oceanography*, **41** (3), 485–502, doi:10.1175/2010JPO4529.
898 1, URL <http://journals.ametsoc.org/doi/abs/10.1175/2010JPO4529.1>.
- 899 Nikurashin, M., G. Vallis, M. Nikurashin, and G. Vallis, 2012: A Theory of the Interhemispheric
900 Meridional Overturning Circulation and Associated Stratification. *Journal of Physical Oceanog-*
901 *raphy*, **42** (10), 1652–1667, doi:10.1175/JPO-D-11-0189.1, URL [http://journals.ametsoc.org/
902 doi/abs/10.1175/JPO-D-11-0189.1](http://journals.ametsoc.org/doi/abs/10.1175/JPO-D-11-0189.1).
- 903 Nycander, J., 2005: Generation of internal waves in the deep ocean by tides. *Journal of Geo-*
904 *physical Research: Oceans*, **110** (C10), doi:10.1029/2004JC002487, URL [https://agupubs.
905 onlinelibrary.wiley.com/doi/abs/10.1029/2004JC002487](https://agupubs.onlinelibrary.wiley.com/doi/abs/10.1029/2004JC002487).
- 906 Osborn, T. R., 1980: Estimates of the Local Rate of Vertical Diffusion from Dissipation Mea-
907 surements. *Journal of Physical Oceanography*, **10** (1), 83–89, doi:10.1175/1520-0485(1980)

908 010(0083:EOTLRO)2.0.CO;2, URL [http://journals.ametsoc.org/doi/abs/10.1175/1520-0485%](http://journals.ametsoc.org/doi/abs/10.1175/1520-0485%281980%29010%3C0083%3AEOTLRO%3E2.0.CO%3B2)
909 [281980%29010%3C0083%3AEOTLRO%3E2.0.CO%3B2](http://journals.ametsoc.org/doi/abs/10.1175/1520-0485%281980%29010%3C0083%3AEOTLRO%3E2.0.CO%3B2).

910 Pedlosky, J., 1992: The Baroclinic Structure of the Abyssal Circulation. *Journal of Physical*
911 *Oceanography*, **22** (6), 652–659, doi:10.1175/1520-0485(1992)022<0652:TBSOTA>2.0.CO;2.

912 Pedlosky, J., 1996: *Ocean Circulation Theory*. Springer Berlin Heidelberg, Berlin, Heidelberg,
913 doi:10.1007/978-3-662-03204-6, URL <http://link.springer.com/10.1007/978-3-662-03204-6>.

914 Phillips, O., 1970: On flows induced by diffusion in a stably stratified fluid. *Deep Sea Research and*
915 *Oceanographic Abstracts*, **17** (3), 435–443, doi:10.1016/0011-7471(70)90058-6, URL [http://](http://linkinghub.elsevier.com/retrieve/pii/0011747170900586)
916 linkinghub.elsevier.com/retrieve/pii/0011747170900586.

917 Phillips, O. M., J.-H. Shyu, and H. Salmun, 1986: An experiment on boundary mixing: mean
918 circulation and transport rates. *Journal of Fluid Mechanics*, **173** (-1), 473, doi:10.1017/
919 S0022112086001234, URL http://www.journals.cambridge.org/abstract_S0022112086001234.

920 Polzin, K., J. Toole, J. R. Ledwell, and R. Schmitt, 1997: Spatial Variability of Turbulent Mix-
921 ing in the Spatial Variability Abyssal Ocean. *Science*, **276** (5309), 93–96, doi:10.1126/science.
922 276.5309.93, URL <http://www.sciencemag.org/cgi/content/abstract/276/5309/93>, iSBN: 0036-
923 8075.

924 Polzin, K. L., 2009: An abyssal recipe. *Ocean Modelling*, **30** (4), 298–309, doi:10.1016/j.ocemod.
925 2009.07.006.

926 Rhines, P. B., 1993: Oceanic General Circulation: Wave and Advection Dynamics. *Modelling*
927 *Oceanic Climate Interactions*, J. Willebrand, and D. L. T. Anderson, Eds., Springer Berlin Hei-
928 delberg, Berlin, Heidelberg, 67–149.

- 929 Robinson, A., and H. Stommel, 1959: The Oceanic Thermocline and the Associated Thermo-
930 haline Circulation. *Tellus*, **11 (3)**, 295–308, doi:10.1111/j.2153-3490.1959.tb00035.x, URL
931 <http://tellusa.net/index.php/tellusa/article/view/9317>, publisher: Wiley/Blackwell (10.1111).
- 932 Salmon, R., 1992: A two-layer Gulf Stream over a continental slope. *Journal of Marine Research*,
933 **50 (3)**, 341–365, doi:10.1357/002224092784797610, URL [http://openurl.ingenta.com/content/
934 xref?genre=article&issn=0022-2402&volume=50&issue=3&spage=341](http://openurl.ingenta.com/content/xref?genre=article&issn=0022-2402&volume=50&issue=3&spage=341).
- 935 Salmon, R., 1998: Linear ocean circulation theory with realistic bathymetry. *Journal of Marine
936 Research*, **56 (4)**, 833–884, doi:10.1357/002224098321667396, URL [http://www.ingentaselect.
937 com/rpsv/cgi-bin/cgi?ini=xref&body=linker&reqdoi=10.1357/002224098321667396](http://www.ingentaselect.com/rpsv/cgi-bin/cgi?ini=xref&body=linker&reqdoi=10.1357/002224098321667396).
- 938 Salmun, H., P. D. Killworth, and J. R. Blundell, 1991: A two-dimensional model of boundary
939 mixing. *Journal of Geophysical Research: Oceans*, **96 (C10)**, 18 447–18 474, doi:10.1029/
940 91JC01917, URL <https://agupubs.onlinelibrary.wiley.com/doi/abs/10.1029/91JC01917>.
- 941 Samelson, R. M., 1998: Large-Scale Circulation with Locally Enhanced Vertical Mixing*.
942 *Journal of Physical Oceanography*, **28 (4)**, 712–726, doi:10.1175/1520-0485(1998)028<0712:
943 LSCWLE>2.0.CO;2, URL [http://journals.ametsoc.org/doi/abs/10.1175/1520-0485%
944 29028%3C0712%3ALSCWLE%3E2.0.CO%3B2](http://journals.ametsoc.org/doi/abs/10.1175/1520-0485%281998%29028%3C0712%3ALSCWLE%3E2.0.CO%3B2).
- 945 Sarmiento, J. L., and J. R. Toggweiler, 1984: A new model for the role of the oceans in determining
946 atmospheric PCO₂. *Nature*, **308 (5960)**, 621–624, doi:10.1038/308621a0, URL [http://www.
947 nature.com/doi/abs/10.1038/308621a0](http://www.nature.com/doi/abs/10.1038/308621a0), publisher: Nature Publishing Group.
- 948 St. Laurent, L., and C. Garrett, 2002: The Role of Internal Tides in Mixing the Deep
949 Ocean. *Journal of Physical Oceanography*, **32 (10)**, 2882–2899, doi:10.1175/1520-0485(2002)

950 032(2882:TROITI)2.0.CO;2, URL [http://journals.ametsoc.org/doi/abs/10.1175/1520-0485%](http://journals.ametsoc.org/doi/abs/10.1175/1520-0485%282002%29032%3C2882%3ATROITI%3E2.0.CO%3B2)
951 [282002%29032%3C2882%3ATROITI%3E2.0.CO%3B2](http://journals.ametsoc.org/doi/abs/10.1175/1520-0485%282002%29032%3C2882%3ATROITI%3E2.0.CO%3B2).

952 St. Laurent, L. C., J. M. Toole, and R. W. Schmitt, 2001: Buoyancy Forcing by Turbulence above
953 Rough Topography in the Abyssal Brazil Basin*. *Journal of Physical Oceanography*, **31** (12),
954 3476–3495, doi:10.1175/1520-0485(2001)031(3476:BFBTAR)2.0.CO;2.

955 Stommel, H., 1948: The westward intensification of wind-driven ocean currents. *Transactions,*
956 *American Geophysical Union*, **29** (2), 202, doi:10.1029/TR029i002p00202, URL [http://doi.](http://doi.wiley.com/10.1029/TR029i002p00202)
957 [wiley.com/10.1029/TR029i002p00202](http://doi.wiley.com/10.1029/TR029i002p00202).

958 Stommel, H., 1957: The Abyssal Circulation of the Ocean. *Nature*, **180** (4589), 733–734, doi:
959 10.1038/180733a0, URL <http://www.nature.com/doi/10.1038/180733a0>.

960 Stommel, H., and A. B. Arons, 1959a: On the abyssal circulation of the world ocean II. An
961 idealized model of the circulation pattern and amplitude in oceanic basins. *Deep Sea Research*
962 (1953), **6**, 217–233, doi:10.1016/0146-6313(59)90075-9, URL [http://www.sciencedirect.com/](http://www.sciencedirect.com/science/article/pii/0146631359900759)
963 [science/article/pii/0146631359900759](http://www.sciencedirect.com/science/article/pii/0146631359900759).

964 Stommel, H., and A. B. Arons, 1959b: On the abyssal circulation of the world oceanI.
965 Stationary planetary flow patterns on a sphere. *Deep Sea Research* (1953), **6**, 140–
966 154, doi:10.1016/0146-6313(59)90065-6, URL [http://www.sciencedirect.com/science/article/](http://www.sciencedirect.com/science/article/pii/0146631359900656)
967 [pii/0146631359900656](http://www.sciencedirect.com/science/article/pii/0146631359900656).

968 Sverdrup, H., M. Johnson, and R. Fleming, 1942: The Oceans: Their Physics, Chemistry
969 and General Biology. *Oceanography*, 1104, doi:10.2307/210609, arXiv: 1011.1669v3 ISBN:
970 9788578110796.

- 971 Talley, L. D., 2007: *Hydrographic atlas of the world ocean circulation experiment (WOCE): Vol-*
972 *ume 2: Pacific Ocean*. WOCE International Project Office Southampton.
- 973 Talley, L. D., 2013a: Closure of the Global Overturning Circulation Through the Indian, Pacific,
974 and Southern Oceans: Schematics and Transports. *Oceanography*, **26 (1)**, 80–97, doi:10.
975 5670/oceanog.2013.07, URL [http://apps.webofknowledge.com/full_record.do?product=UA&](http://apps.webofknowledge.com/full_record.do?product=UA&search_mode=GeneralSearch&qid=14&SID=W1jPgx8kkS6brME6NvD&page=1&doc=1)
976 [search_mode=GeneralSearch&qid=14&SID=W1jPgx8kkS6brME6NvD&page=1&doc=1,](http://apps.webofknowledge.com/full_record.do?product=UA&search_mode=GeneralSearch&qid=14&SID=W1jPgx8kkS6brME6NvD&page=1&doc=1)
977 arXiv: 1011.1669v3 ISBN: 1042-8275.
- 978 Talley, L. D., 2013b: *Hydrographic Atlas of the World Ocean Circulation Experiment (WOCE):*
979 *volume 4: Indian Ocean*. International WOCE Project Office.
- 980 Thompson, A. F., A. L. Stewart, and T. Bischoff, 2016: A Multibasin Residual-Mean Model for
981 the Global Overturning Circulation. *Journal of Physical Oceanography*, **46 (9)**, 2583–2604, doi:
982 10.1175/JPO-D-15-0204.1, URL <http://journals.ametsoc.org/doi/10.1175/JPO-D-15-0204.1>.
- 983 Thorpe, S. A., 1987: Current and Temperature Variability on the Continental Slope. *Philosoph-*
984 *ical Transactions of the Royal Society A: Mathematical, Physical and Engineering Sciences*,
985 **323 (1574)**, 471–517, doi:10.1098/rsta.1987.0100, URL [http://rsta.royalsocietypublishing.org/](http://rsta.royalsocietypublishing.org/cgi/doi/10.1098/rsta.1987.0100)
986 [cgi/doi/10.1098/rsta.1987.0100](http://rsta.royalsocietypublishing.org/cgi/doi/10.1098/rsta.1987.0100), publisher: The Royal Society.
- 987 Thurnherr, A. M., and K. G. Speer, 2003: Boundary Mixing and Topographic Blocking on the
988 Mid-Atlantic Ridge in the South Atlantic*. *Journal of Physical Oceanography*, **33 (4)**, 848–
989 862, doi:10.1175/1520-0485(2003)33<848:BMATBO>2.0.CO;2, URL [http://journals.ametsoc.](http://journals.ametsoc.org/doi/abs/10.1175/1520-0485%282003%2933%3C848%3ABMATBO%3E2.0.CO%3B2)
990 [org/doi/abs/10.1175/1520-0485%282003%2933%3C848%3ABMATBO%3E2.0.CO%3B2](http://journals.ametsoc.org/doi/abs/10.1175/1520-0485%282003%2933%3C848%3ABMATBO%3E2.0.CO%3B2).
- 991 Thurnherr, A. M., and Coauthors, 2005: Mixing Associated with Sills in a Canyon on the Mi-
992 docean Ridge Flank*. *Journal of Physical Oceanography*, **35 (8)**, 1370–1381, doi:10.1175/

993 JPO2773.1, URL <http://journals.ametsoc.org/doi/abs/10.1175/JPO2773.1>.

994 Toggweiler, J. R., K. Dixon, and K. Bryan, 1989: Simulations of radiocarbon in a coarse-
995 resolution world ocean model: 1. Steady state prebomb distributions. *Journal of Geophysical*
996 *Research*, **94 (C6)**, 8217, doi:10.1029/JC094iC06p08217, URL [http://doi.wiley.com/10.1029/](http://doi.wiley.com/10.1029/JC094iC06p08217)
997 [JC094iC06p08217](http://doi.wiley.com/10.1029/JC094iC06p08217).

998 Walin, G., 1982: On the relation between sea-surface heat flow and thermal circulation in the
999 ocean. *Tellus*, **34 (2)**, 187–195, doi:10.1111/j.2153-3490.1982.tb01806.x, URL [http://tellusa.](http://tellusa.net/index.php/tellusa/article/view/10801)
1000 [net/index.php/tellusa/article/view/10801](http://tellusa.net/index.php/tellusa/article/view/10801), publisher: Wiley/Blackwell (10.1111).

1001 Waterhouse, A. F., and Coauthors, 2014: Global Patterns of Diapycnal Mixing from Measurements
1002 of the Turbulent Dissipation Rate. *Journal of Physical Oceanography*, **44 (7)**, 1854–1872, doi:
1003 10.1175/JPO-D-13-0104.1, URL [http://journals.ametsoc.org/doi/abs/10.1175/JPO-D-13-0104.](http://journals.ametsoc.org/doi/abs/10.1175/JPO-D-13-0104.1)
1004 [1](http://journals.ametsoc.org/doi/abs/10.1175/JPO-D-13-0104.1), iISBN: 0022-3670.

1005 Wunsch, C., 1970: On oceanic boundary mixing. *Deep-Sea Research and Oceanographic Ab-*
1006 *stracts*, **17 (2)**, 293–301, doi:10.1016/0011-7471(70)90022-7.

LIST OF FIGURES

| | | |
|------|----------------|--|
| 1007 | | |
| 1008 | Fig. 1. | Schematic of an abyssal circulation driven by near-boundary mixing. Dense bottom waters flow northward out of the Southern Ocean via a deep western boundary current (red circle) along the smooth and relatively quiescent continental slope, where little watermass transformation occurs. A cross-basin zonal flow feeds bottom waters from the deep western boundary current into a system of bottom mixing layers driven by bottom-enhanced turbulent mixing (squiggly orange arrows) generated by flow interactions with rough topography on the flanks of a mid-ocean ridge. The turbulent buoyancy flux converges in a bottom boundary layer (BBL), driving vigorous diabatic upwelling. In a stratified mixing layer (SML) above, the buoyancy flux diverges, driving diabatic downwelling. The net effect of the up- and down-welling in the bottom mixing layers is a net transformation of bottom waters into deep waters. The newly formed deep waters return via cross-basin zonal flows to the smooth continental slope, wherein they flow southward in a deep western boundary current (blue circles) to close the abyssal circulation in the Southern Ocean. 53 |
| 1009 | | |
| 1010 | | |
| 1011 | | |
| 1012 | | |
| 1013 | | |
| 1014 | | |
| 1015 | | |
| 1016 | | |
| 1017 | | |
| 1018 | | |
| 1019 | | |
| 1020 | | |
| 1021 | Fig. 2. | Configuration of the Planetary Geostrophic Circulation Model (PGCM). (a) Seafloor depth in the PGCM. We highlight the southern restoring region where we apply a buoyancy restoring which acts to transform deep waters into bottom waters (see Section 3c) and a northern-hemisphere region in which we diagnose watermass transformations along the mid-ocean ridge (see Section 4c). (b) Zonal section of the imposed turbulent diffusivity κ , which is bottom-enhanced over the mid-ocean ridge. (c) The red lines show the four stratification profiles B_z used in the PGCM as both the initial condition and as the reference profile for buoyancy restoring in the southern restoring region. The black line shows the observed stratification profile from the World Ocean Circulation Experiment (Gouretski and Koltermann 2004) in the South Pacific, averaged horizontally from 55°S to 45°S and 175°E to 115°W. 54 |
| 1022 | | |
| 1023 | | |
| 1024 | | |
| 1025 | | |
| 1026 | | |
| 1027 | | |
| 1028 | | |
| 1029 | | |
| 1030 | | |
| 1031 | Fig. 3. | Cartesian components of the velocity vector in the PGCM-REAL simulation along: (a-c) a mid-latitude section in the northern hemisphere, $y = 3000$ km, and (d-f) a section at the equator, $y = 0$ km. Black lines show three equally spaced buoyancy surfaces. 55 |
| 1032 | | |
| 1033 | | |
| 1034 | Fig. 4. | (a) Meridional, (b) barotropic, and (c) zonal overturning circulations in the PGCM-REAL simulation (see definitions in Section 4b). In all cases, positive values correspond to clockwise circulations. The red and blue solid lines in (a) and (c), respectively, show the height of the mid-ocean ridge along the dashed lines of the same colors in (b). The thick black lines in (b) are the 3000 m and 4000 m isobaths, which highlight both the continental slopes and the the mid-ocean ridge. The thin black lines in (a) and (c) are equally-spaced buoyancy surfaces. 56 |
| 1035 | | |
| 1036 | | |
| 1037 | | |
| 1038 | | |
| 1039 | | |
| 1040 | | |
| 1041 | Fig. 5. | Watermass transformations from the PGCM-REAL simulation in (a) the full northern hemisphere basin ($y > 0$), (b) along the northern-hemisphere mid-ocean ridge ($y > 0$, $L/2 < x < 3L/2$), and (c) in a limited watermass analysis region along the northern-hemisphere mid-ocean ridge ($0 < y < L/2$, $L/2 < x < 3L/2$) highlighted in Figures 2 and 12. The black line shows the net watermass transformation, defined by equation (18). The red and blue lines show the contributions from the bottom boundary layer (BBL) and the stratified mixing layer above (SML). The dashed lines show the contributions from only the vertical component of the buoyancy flux. All watermass transformations in the paper are computed in buoyancy space and remapped into depth space (according to eq. 19) for convenient inter-comparison across simulations with dramatically different stratification and with the fixed depths of topographic features. 57 |
| 1042 | | |
| 1043 | | |
| 1044 | | |
| 1045 | | |
| 1046 | | |
| 1047 | | |
| 1048 | | |
| 1049 | | |
| 1050 | | |
| 1051 | | |
| 1052 | Fig. 6. | Vertical velocity (colors) and buoyancy surfaces (black lines) in bottom mixing layers along a zonal section that crosses the mid-ocean ridge in (a,c) the 1D PGCM emulator and (b,d) |
| 1053 | | |

1054 the full 3D PGCM, where both are initialized from identical constant stratification buoyancy
 1055 fields. The top row shows the solutions at an initial time $\hat{t} = 0.1$, at which point the bottom
 1056 mixing layers have spun up but the basin-scale circulation has not (see Section 3d). The
 1057 bottom row shows the solution at $\hat{t} = 50$, at which point the full solution has roughly come
 1058 to equilibrium with the buoyancy restoring in the Southern Ocean. The predicted buoyancy
 1059 surfaces in (a,c) are reproduced as dashed grey lines in (b,d) to show how the 1D emulator
 1060 predicts the buoyancy field well for short times but that the interior stratification in the
 1061 PGCM drifts far from the 1D emulator’s prediction as it approaches equilibrium. 58

1062 **Fig. 7.** Temporal evolution of the horizontally-averaged northern hemisphere stratification in
 1063 PGCM simulations. Solid lines show the evolution for simulations with a constant strati-
 1064 fication reference buoyancy profile and dashed lines show the evolution for simulations with
 1065 a reference buoyancy profile corresponding to stratification that decays with depth with a
 1066 scale height of 1000 m. The ridge height is varied from $r_h = 1000$ m in (a) and $r_h = 2000$ m
 1067 in (b), as indicated by the dashed brown line. In all cases the equilibrium stratification drifts
 1068 away from the reference profile; however, the equilibrium stratification for constant strati-
 1069 fication is much more different from the reference profile than for the exponential reference
 1070 profile. 59

1071 **Fig. 8.** Watermass transformations in: (a, e) a 1D emulator of the PGCM and (b-d, f-h) the 3D
 1072 PGCM simulations with reference buoyancy profiles corresponding to stratification profiles
 1073 with exponential scale height δ (we recover $N^2 = \text{constant}$ as $\delta \rightarrow \infty$). The initial spin-up
 1074 at $\hat{t} = 0.1$ is shown in (a-d) and the equilibrium state at $\hat{t} = 50$ is show in (e-h). Black,
 1075 red, and blue lines show the net, bottom boundary layer (BBL), and stratified mixing layer
 1076 (SML) contributions to the watermass transformations, respectively. The black dashed line
 1077 in (a,e) shows the integral constraint $L\Psi_\infty = L\kappa_{bg} \cot \theta_{\max}$ derived from boundary layer the-
 1078 ory, where we take θ_{\max} as the maximum slope angle in the domain. The brown dashed line
 1079 marks the depth of the ridge crest. 60

1080 **Fig. 9.** Scaling of watermass transformations in mixing layers with (a) the height δ over which the
 1081 restoring stratification varies and (b) the bottom diffusivity κ_{bot} . Colored symbols represent
 1082 the absolute value of the maximum transport in the BBL (red), the SML (blue), and the
 1083 net (black), with squares and diamonds representing the PGCM-CONST and PGCM-REAL
 1084 simulations, respectively. The grey shading in (a) represents realistic vertical scales over
 1085 which abyssal stratification varies. The dashed brown line in (c) represents the height of
 1086 ridge. In all experiments, the maximum net and BBL transformations occur at depths of
 1087 roughly 4250 m, at the base of the ridge slope, while the maximum BBL transformation
 1088 occurs at the ridge crest. 61

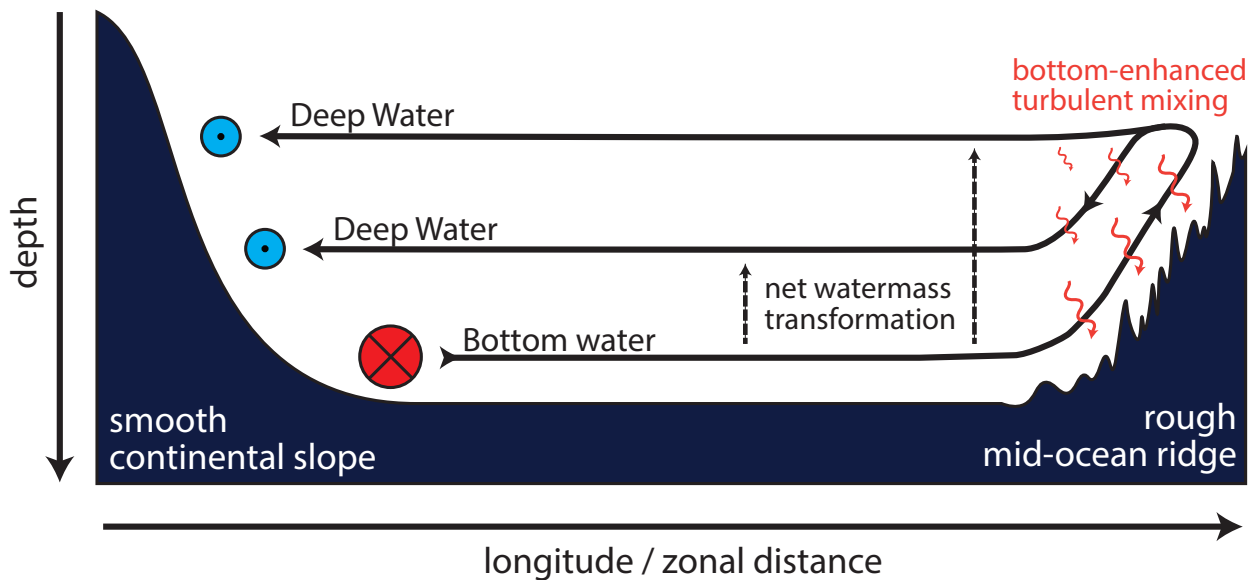
1089 **Fig. 10.** Watermass transformations in PGCM simulations as a function of ridge height. All panels
 1090 are for a fixed constant stratification reference buoyancy profile. The initial spin-up at $\hat{t} = 0.1$
 1091 is shown in (a-d) and the equilibrium state at $\hat{t} = 50$ is shown in (e-h). Mid-ocean ridge height
 1092 increases in increments of 500 m from left to right, as indicated by the dashed brown lines.
 1093 Black, red, and blue lines show the net, bottom boundary layer (BBL), and stratified mixing
 1094 layer (SML) contributions to the watermass transformations, respectively. 62

1095 **Fig. 11.** Diabatic zonal overturning circulation driven by bottom-enhanced mixing on the western
 1096 flank of a mid-ocean ridge in (a) the South Atlantic Ocean and (b) the PGCM-REAL simu-
 1097 lation. White lines show arbitrarily chosen contours of the counter-clockwise zonal over-
 1098 turning streamfunction, where the values for (a) are digitized from Figure 14 of St. Laurent
 1099 et al. (2001) and for (b) are diagnosed from PGCM-REAL simulation. Coloring shows the
 1100 vertical diffusivity in log-scale (light-grey shading represents depths with no microstructure
 1101 measurements and does not necessarily represent topography), where panel (a) is inspired

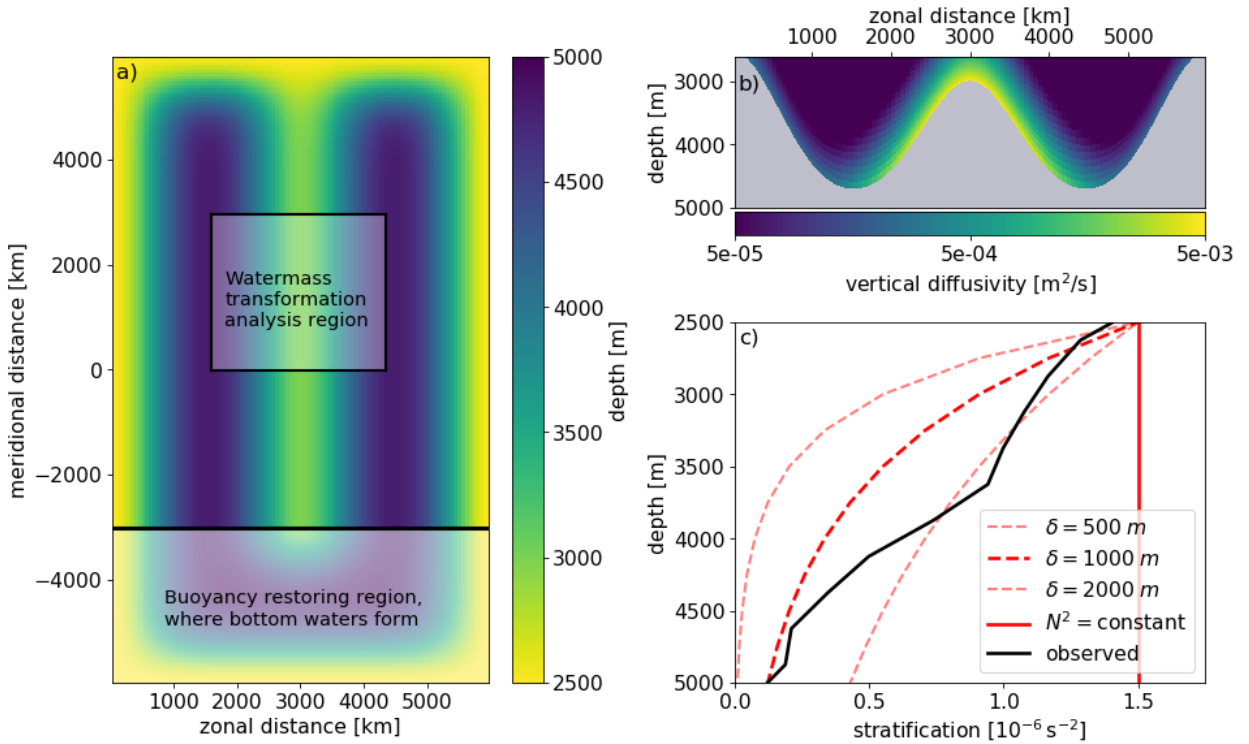
1102 by Figure 2 of Polzin et al. (1997) and the diffusivity is calculated with microstructure pro-
 1103 files from the BBTRE experiment (archived at microstructure.ucsd.edu). Black lines are:
 1104 (a) potential density σ_4 surfaces (referenced to 4000 m) from the microstructure profiles and
 1105 (b) buoyancy surfaces from the PGCM solution, chosen arbitrarily to show that the zonal
 1106 overturning circulation is indeed diabatic. The dark grey lines in (a) show the depth mini-
 1107 mum (canyon floor) and maximum (canyon crest) seafloor depth within 0.5° latitude of the
 1108 microstructure profiles. In (b), zonal distance along the PGCM section has been converted
 1109 to an equivalent longitude at 25°S so that length scales can be directly compared between
 1110 the two panels. 63

1111 **Fig. 12.** (a-d) Watermass transformations at all abyssal depths and (e,f) buoyancy flux convergence
 1112 at 3250 m depth in similarly-sized domains containing mid-ocean ridges, as diagnosed from
 1113 (a,e) the PGCM-REAL simulation and estimated for the (b,f) Pacific, (c,f) Atlantic, and
 1114 (d,f) Indian Oceans. In (a-d), the black, red, and blue lines show the net, bottom boundary
 1115 layer (BBL), and stratified mixing layer (SML) contributions to the watermass transfor-
 1116 mations, respectively (grey shaded indicates depths representing very little ocean volume). The
 1117 black boxes in (e,f) delineate the similarly-sized regions (each with dimensions of roughly
 1118 $3000\text{ km} \times 3000\text{ km}$) for which we compute the watermass transformations. In (e,f), red and
 1119 blue show regions of buoyancy flux convergence (positive buoyancy tendency) and buoy-
 1120 ancy flux divergence (negative buoyancy tendency), respectively. 64

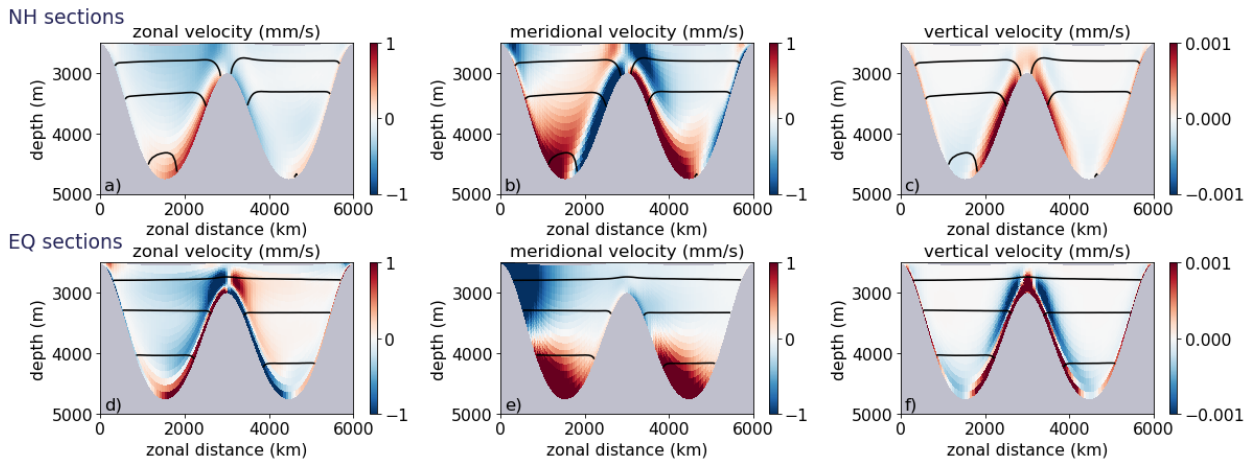
1121 **Fig. 13.** Comparing diagnostics of abyssal upwelling in PGCM simulations for the watermass trans-
 1122 formation analysis region highlighted in Figure 2a. The first row (a-d), second row (e-h),
 1123 and third row (i-l) represent three equilibrium experiments with different ridge height r_h and
 1124 stratification scale height δ . The solid blue line in column (d,h,l) represents Munk and Wun-
 1125 sch (1998)’s estimate for the abyssal upwelling transport $\langle w \rangle A \simeq \frac{A(z)}{\langle N^2 \rangle} \frac{d}{dz} [\langle \kappa \rangle \langle N^2 \rangle]$ (eq. 24),
 1126 which is an extension of Munk (1966)’s classic point-wise vertical advection-diffusion to a
 1127 basin-wide average that also accounts for changes in isobath surface area with depth. The
 1128 first three columns show the individual variables in the Munk and Wunsch (1998) expres-
 1129 sion: (a,e,i) the horizontally-averaged stratification $\langle N^2 \rangle$, (b,f,j) the horizontally-averaged
 1130 diffusivity $\langle \kappa \rangle$, and (c,g,k) isobath surface area $A(z)$. The dashed black line shows the up-
 1131 welling transport $\langle w \rangle A$ diagnosed directly from the simulated velocity field. The solid black
 1132 line shows the net watermass transformation, where its native density coordinate has been
 1133 mapped into a pseudo-depth coordinate by taking the average depth of a given buoyancy
 1134 surface (eq. 19). For all of our simulations of abyssal circulations driven by near-boundary
 1135 mixing, the Munk and Wunsch (1998) expression is a poor substitute for watermass trans-
 1136 formations, which themselves agree favorably with the diagnosed vertical transport $\langle w \rangle A$.
 1137 65



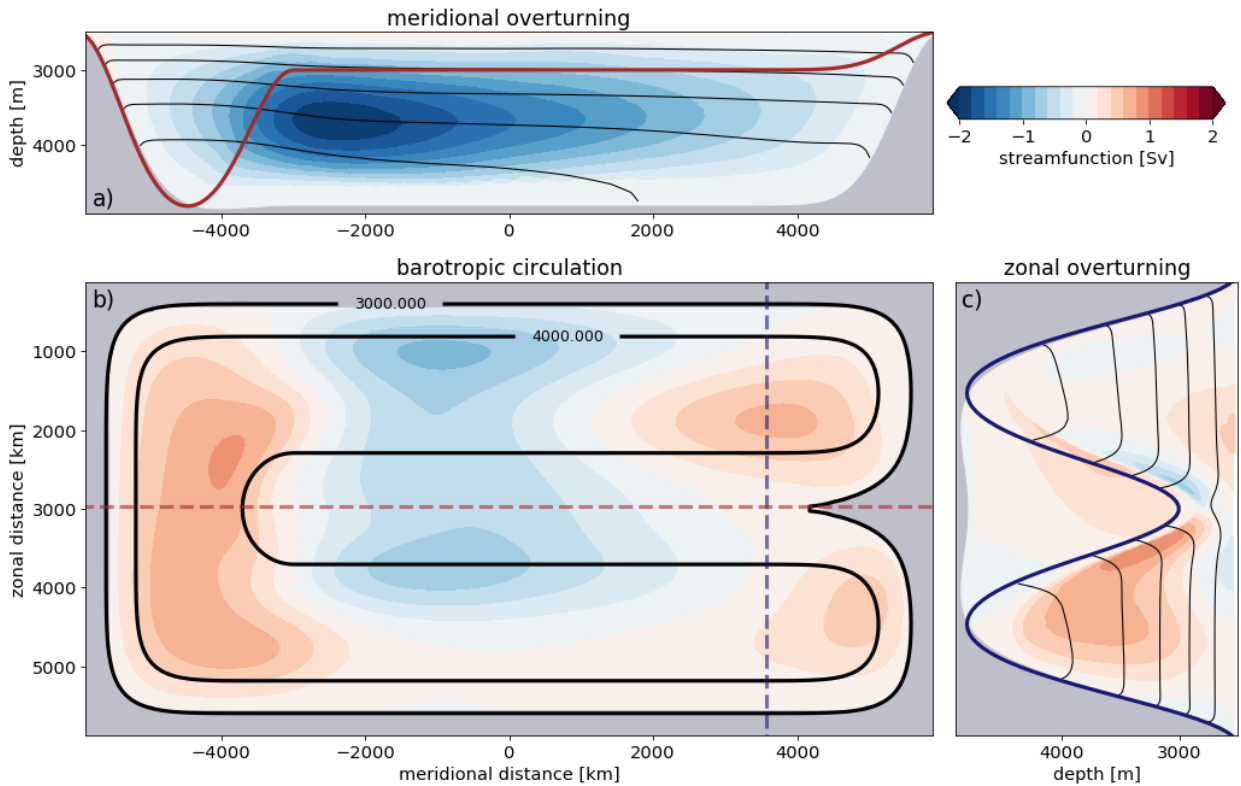
1138 FIG. 1. Schematic of an abyssal circulation driven by near-boundary mixing. Dense bottom waters flow
 1139 northward out of the Southern Ocean via a deep western boundary current (red circle) along the smooth and
 1140 relatively quiescent continental slope, where little watermass transformation occurs. A cross-basin zonal flow
 1141 feeds bottom waters from the deep western boundary current into a system of bottom mixing layers driven by
 1142 bottom-enhanced turbulent mixing (squiggly orange arrows) generated by flow interactions with rough topog-
 1143 raphy on the flanks of a mid-ocean ridge. The turbulent buoyancy flux converges in a bottom boundary layer
 1144 (BBL), driving vigorous diabatic upwelling. In a stratified mixing layer (SML) above, the buoyancy flux di-
 1145 verges, driving diabatic downwelling. The net effect of the up- and down-welling in the bottom mixing layers
 1146 is a net transformation of bottom waters into deep waters. The newly formed deep waters return via cross-basin
 1147 zonal flows to the smooth continental slope, wherein they flow southward in a deep western boundary current
 1148 (blue circles) to close the abyssal circulation in the Southern Ocean.



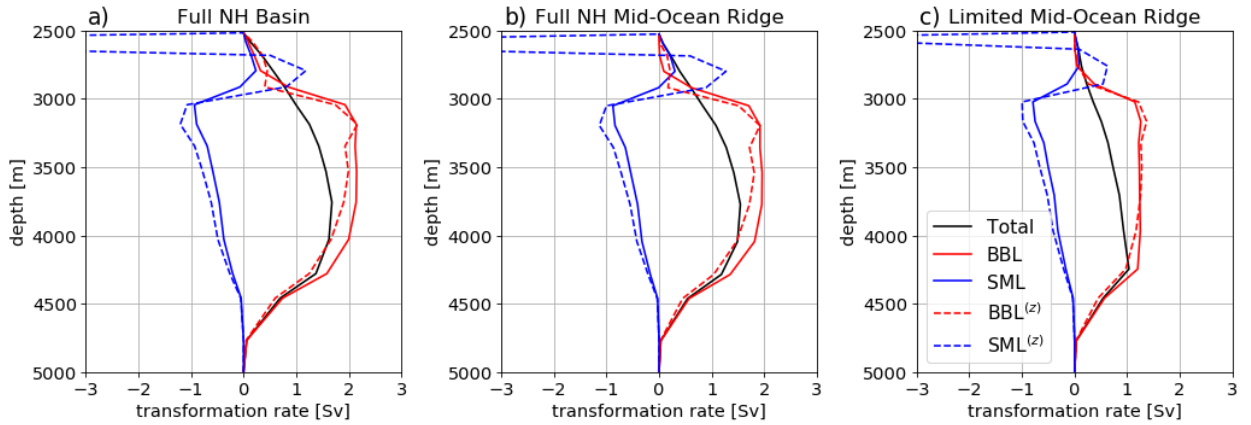
1149 FIG. 2. Configuration of the Planetary Geostrophic Circulation Model (PGCM). (a) Seafloor depth in the
 1150 PGCM. We highlight the southern restoring region where we apply a buoyancy restoring which acts to transform
 1151 deep waters into bottom waters (see Section 3c) and a northern-hemisphere region in which we diagnose wa-
 1152 termass transformations along the mid-ocean ridge (see Section 4c). (b) Zonal section of the imposed turbulent
 1153 diffusivity κ , which is bottom-enhanced over the mid-ocean ridge. (c) The red lines show the four stratification
 1154 profiles B_z used in the PGCM as both the initial condition and as the reference profile for buoyancy restoring
 1155 in the southern restoring region. The black line shows the observed stratification profile from the World Ocean
 1156 Circulation Experiment (Gouretski and Koltermann 2004) in the South Pacific, averaged horizontally from 55°S
 1157 to 45°S and 175°E to 115°W.



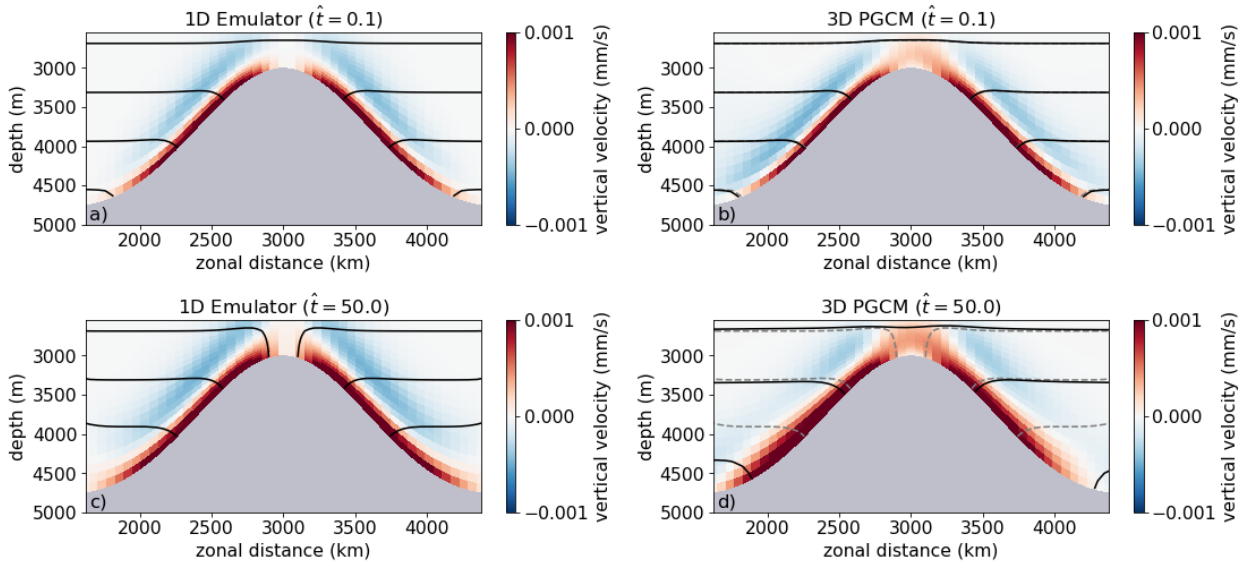
1158 FIG. 3. Cartesian components of the velocity vector in the PGCM-REAL simulation along: (a-c) a mid-
 1159 latitude section in the northern hemisphere, $y = 3000$ km, and (d-f) a section at the equator, $y = 0$ km. Black
 1160 lines show three equally spaced buoyancy surfaces.



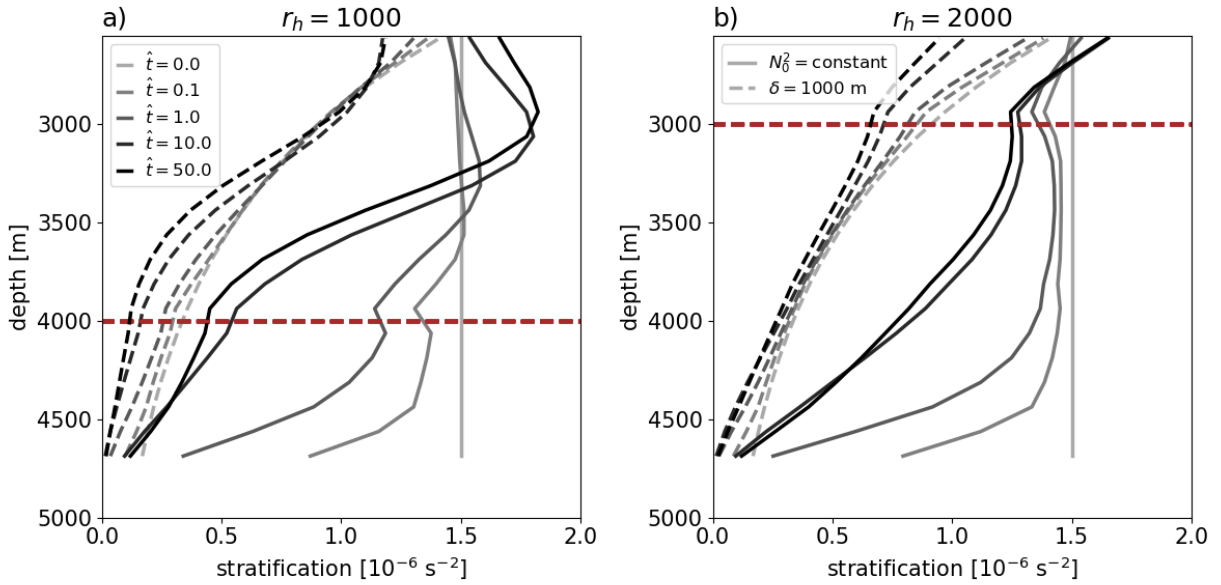
1161 FIG. 4. (a) Meridional, (b) barotropic, and (c) zonal overturning circulations in the PGCM-REAL simulation
 1162 (see definitions in Section 4b). In all cases, positive values correspond to clockwise circulations. The red and
 1163 blue solid lines in (a) and (c), respectively, show the height of the mid-ocean ridge along the dashed lines of the
 1164 same colors in (b). The thick black lines in (b) are the 3000 m and 4000 m isobaths, which highlight both the
 1165 continental slopes and the the mid-ocean ridge. The thin black lines in (a) and (c) are equally-spaced buoyancy
 1166 surfaces.



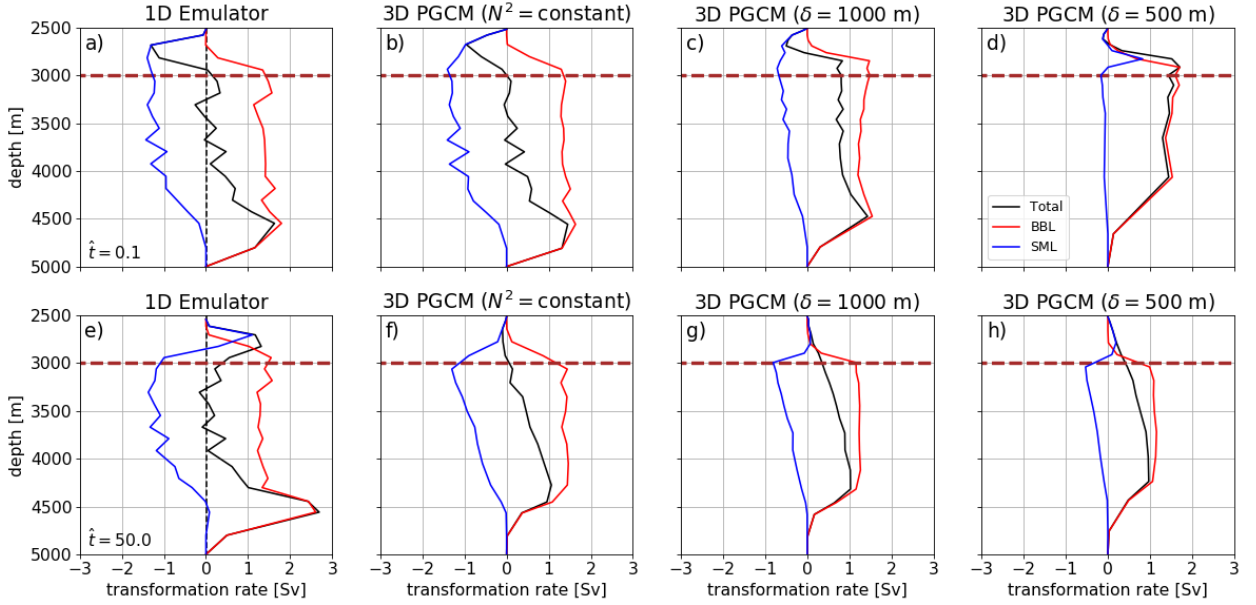
1167 FIG. 5. Watermass transformations from the PGCM-REAL simulation in (a) the full northern hemisphere
 1168 basin ($y > 0$), (b) along the northern-hemisphere mid-ocean ridge ($y > 0, L/2 < x < 3L/2$), and (c) in a limited
 1169 watermass analysis region along the northern-hemisphere mid-ocean ridge ($0 < y < L/2, L/2 < x < 3L/2$)
 1170 highlighted in Figures 2 and 12. The black line shows the net watermass transformation, defined by equation
 1171 (18). The red and blue lines show the contributions from the bottom boundary layer (BBL) and the stratified
 1172 mixing layer above (SML). The dashed lines show the contributions from only the vertical component of the
 1173 buoyancy flux. All watermass transformations in the paper are computed in buoyancy space and remapped into
 1174 depth space (according to eq. 19) for convenient inter-comparison across simulations with dramatically different
 1175 stratification and with the fixed depths of topographic features.



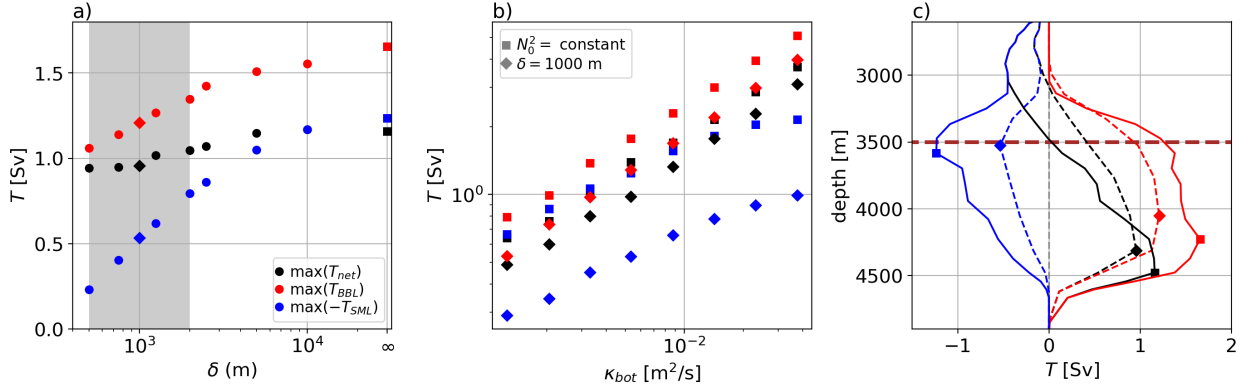
1176 FIG. 6. Vertical velocity (colors) and buoyancy surfaces (black lines) in bottom mixing layers along a zonal
 1177 section that crosses the mid-ocean ridge in (a,c) the 1D PGCM emulator and (b,d) the full 3D PGCM, where
 1178 both are initialized from identical constant stratification buoyancy fields. The top row shows the solutions at an
 1179 initial time $\hat{t} = 0.1$, at which point the bottom mixing layers have spun up but the basin-scale circulation has
 1180 not (see Section 3d). The bottom row shows the solution at $\hat{t} = 50$, at which point the full solution has roughly
 1181 come to equilibrium with the buoyancy restoring in the Southern Ocean. The predicted buoyancy surfaces in
 1182 (a,c) are reproduced as dashed grey lines in (b,d) to show how the 1D emulator predicts the buoyancy field well
 1183 for short times but that the interior stratification in the PGCM drifts far from the 1D emulator's prediction as it
 1184 approaches equilibrium.



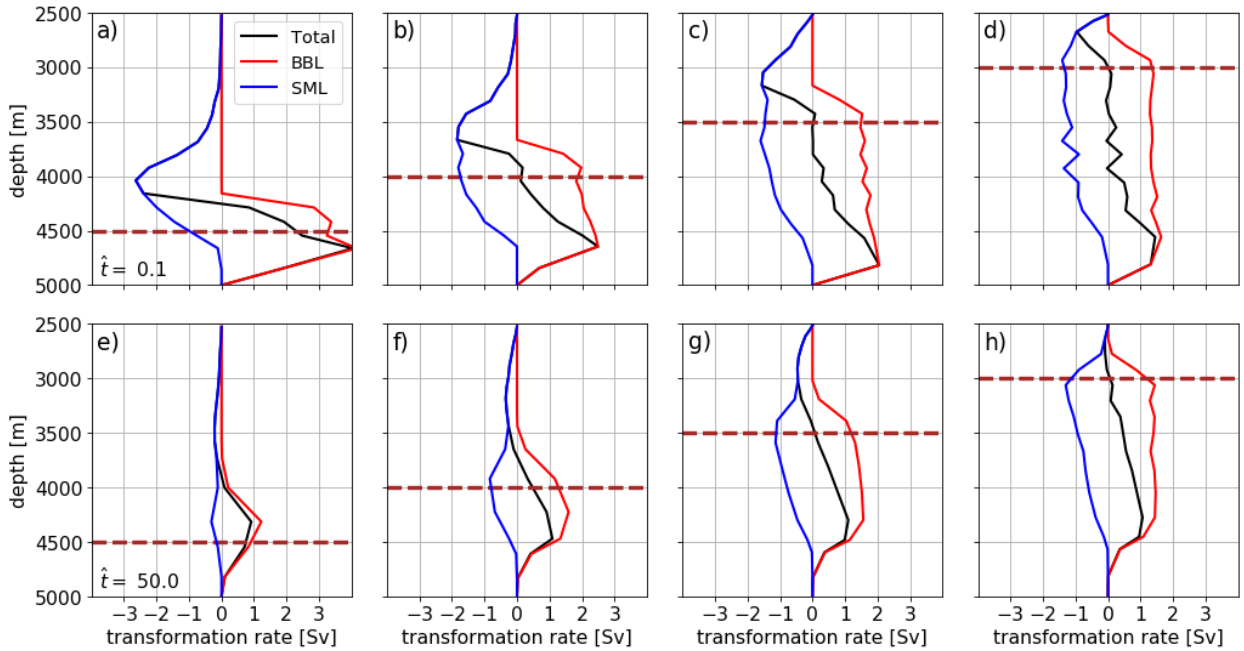
1185 FIG. 7. Temporal evolution of the horizontally-averaged northern hemisphere stratification in PGCM simu-
 1186 lations. Solid lines show the evolution for simulations with a constant stratification reference buoyancy profile
 1187 and dashed lines show the evolution for simulations with a reference buoyancy profile corresponding to stratifi-
 1188 cation that decays with depth with a scale height of 1000 m. The ridge height is varied from $r_h = 1000$ m in (a)
 1189 and $r_h = 2000$ m in (b), as indicated by the dashed brown line. In all cases the equilibrium stratification drifts
 1190 away from the reference profile; however, the equilibrium stratification for constant stratification is much more
 1191 different from the reference profile than for the exponential reference profile.



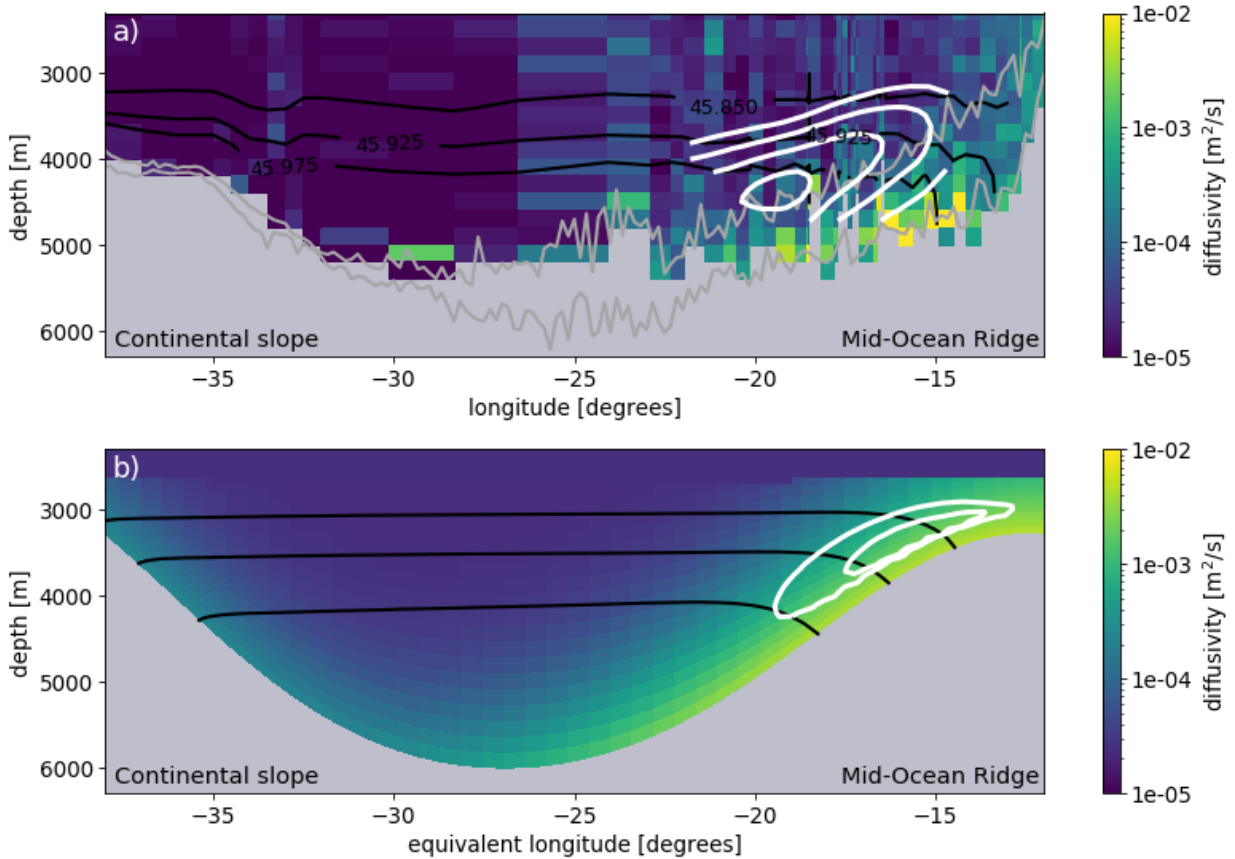
1192 FIG. 8. Watermass transformations in: (a, e) a 1D emulator of the PGCM and (b-d, f-h) the 3D PGCM simu-
 1193 lations with reference buoyancy profiles corresponding to stratification profiles with exponential scale height δ
 1194 (we recover $N^2 = \text{constant}$ as $\delta \rightarrow \infty$). The initial spin-up at $\hat{t} = 0.1$ is shown in (a-d) and the equilibrium state
 1195 at $\hat{t} = 50$ is shown in (e-h). Black, red, and blue lines show the net, bottom boundary layer (BBL), and stratified
 1196 mixing layer (SML) contributions to the watermass transformations, respectively. The black dashed line in (a,e)
 1197 shows the integral constraint $L\Psi_\infty = L\kappa_{bg} \cot \theta_{\max}$ derived from boundary layer theory, where we take θ_{\max} as
 1198 the maximum slope angle in the domain. The brown dashed line marks the depth of the ridge crest.



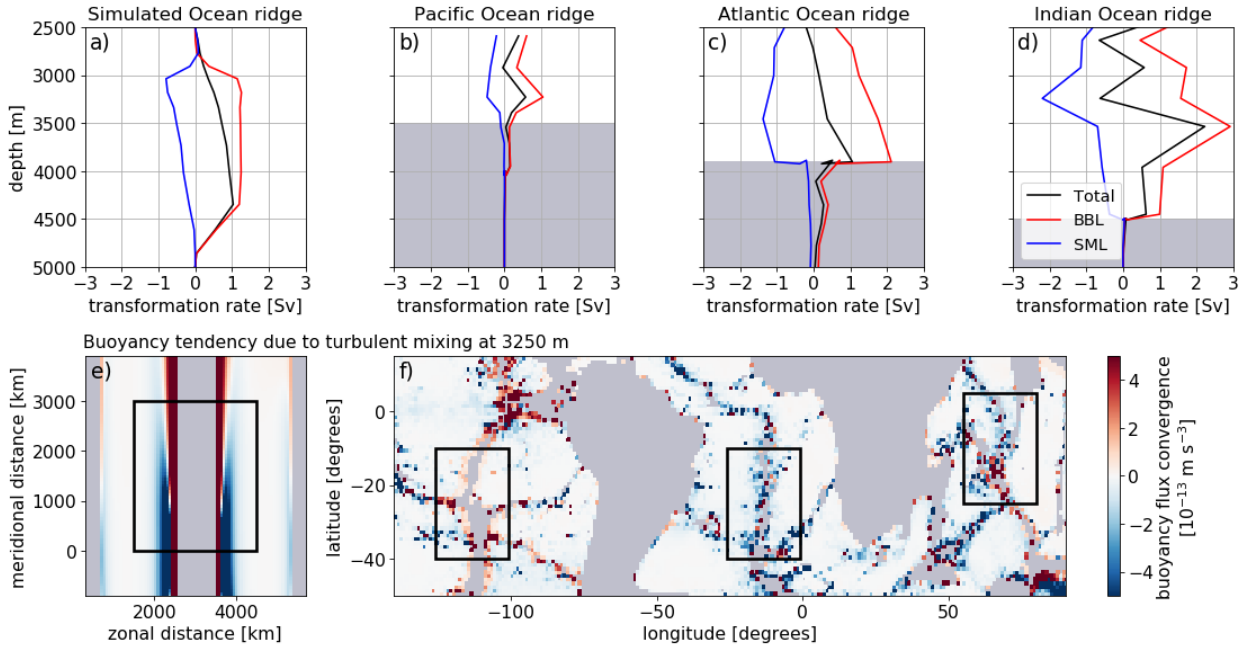
1199 FIG. 9. Scaling of watermass transformations in mixing layers with (a) the height δ over which the restoring
 1200 stratification varies and (b) the bottom diffusivity κ_{bot} . Colored symbols represent the absolute value of the max-
 1201 imum transport in the BBL (red), the SML (blue), and the net (black), with squares and diamonds representing
 1202 the PGCM-CONST and PGCM-REAL simulations, respectively. The grey shading in (a) represents realistic
 1203 vertical scales over which abyssal stratification varies. The dashed brown line in (c) represents the height of
 1204 ridge. In all experiments, the maximum net and BBL transformations occur at depths of roughly 4250 m, at the
 1205 base of the ridge slope, while the maximum BBL transformation occurs at the ridge crest.



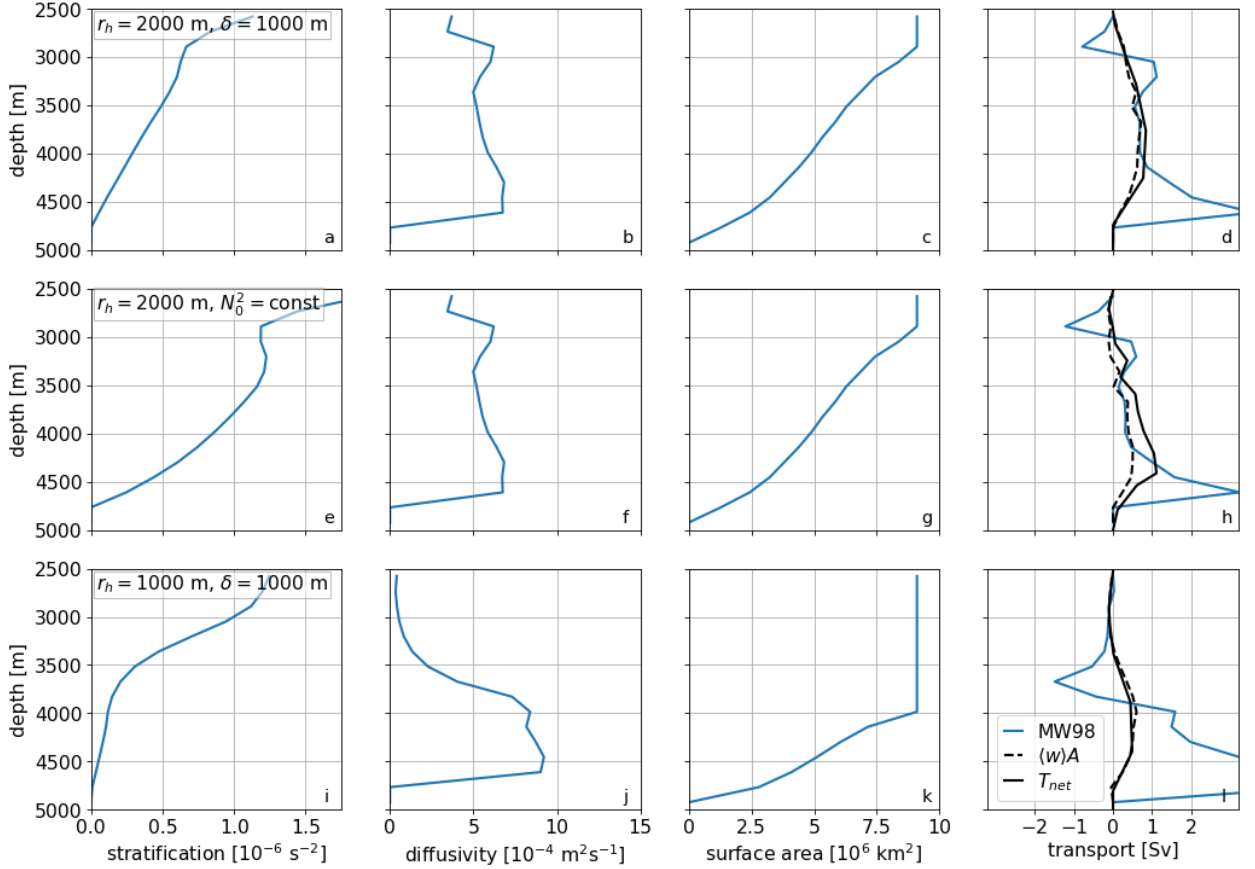
1206 FIG. 10. Watermass transformations in PGCM simulations as a function of ridge height. All panels are for a
 1207 fixed constant stratification reference buoyancy profile. The initial spin-up at $\hat{t} = 0.1$ is shown in (a-d) and the
 1208 equilibrium state at $\hat{t} = 50$ is shown in (e-h). Mid-ocean ridge height increases in increments of 500 m from left
 1209 to right, as indicated by the dashed brown lines. Black, red, and blue lines show the net, bottom boundary layer
 1210 (BBL), and stratified mixing layer (SML) contributions to the watermass transformations, respectively.



1211 FIG. 11. Diabatic zonal overturning circulation driven by bottom-enhanced mixing on the western flank of
 1212 a mid-ocean ridge in (a) the South Atlantic Ocean and (b) the PGCM-REAL simulation. White lines show
 1213 arbitrarily chosen contours of the counter-clockwise zonal overturning streamfunction, where the values for (a)
 1214 are digitized from Figure 14 of St. Laurent et al. (2001) and for (b) are diagnosed from PGCM-REAL simulation.
 1215 Coloring shows the vertical diffusivity in log-scale (light-grey shading represents depths with no microstructure
 1216 measurements and does not necessarily represent topography), where panel (a) is inspired by Figure 2 of Polzin
 1217 et al. (1997) and the diffusivity is calculated with microstructure profiles from the BBTRE experiment (archived
 1218 at microstructure.ucsd.edu). Black lines are: (a) potential density σ_4 surfaces (referenced to 4000 m) from the
 1219 microstructure profiles and (b) buoyancy surfaces from the PGCM solution, chosen arbitrarily to show that the
 1220 zonal overturning circulation is indeed diabatic. The dark grey lines in (a) show the depth minimum (canyon
 1221 floor) and maximum (canyon crest) seafloor depth within 0.5° latitude of the microstructure profiles. In (b),
 1222 zonal distance along the PGCM section has been converted to an equivalent longitude at 25°S so that length
 1223 scales can be directly compared between the two panels.



1224 FIG. 12. (a-d) Watermass transformations at all abyssal depths and (e,f) buoyancy flux convergence at 3250 m
 1225 depth in similarly-sized domains containing mid-ocean ridges, as diagnosed from (a,e) the PGCM-REAL simu-
 1226 lation and estimated for the (b,f) Pacific, (c,f) Atlantic, and (d,f) Indian Oceans. In (a-d), the black, red, and blue
 1227 lines show the net, bottom boundary layer (BBL), and stratified mixing layer (SML) contributions to the wa-
 1228 termass transformations, respectively (grey shaded indicates depths representing very little ocean volume). The
 1229 black boxes in (e,f) delineate the similarly-sized regions (each with dimensions of roughly $3000 \text{ km} \times 3000 \text{ km}$)
 1230 for which we compute the watermass transformations. In (e,f), red and blue show regions of buoyancy flux
 1231 convergence (positive buoyancy tendency) and buoyancy flux divergence (negative buoyancy tendency), respec-
 1232 tively.



1233 FIG. 13. Comparing diagnostics of abyssal upwelling in PGCM simulations for the watermass transforma-
 1234 tion analysis region highlighted in Figure 2a. The first row (a-d), second row (e-h), and third row (i-l) repre-
 1235 sent three equilibrium experiments with different ridge height r_h and stratification scale height δ . The solid
 1236 blue line in column (d,h,l) represents Munk and Wunsch (1998)’s estimate for the abyssal upwelling trans-
 1237 port $\langle w \rangle A \simeq \frac{A(z)}{\langle N^2 \rangle} \frac{d}{dz} [\langle \kappa \rangle \langle N^2 \rangle]$ (eq. 24), which is an extension of Munk (1966)’s classic point-wise vertical
 1238 advection-diffusion to a basin-wide average that also accounts for changes in isobath surface area with depth.
 1239 The first three columns show the individual variables in the Munk and Wunsch (1998) expression: (a,e,i) the
 1240 horizontally-averaged stratification $\langle N^2 \rangle$, (b,f,j) the horizontally-averaged diffusivity $\langle \kappa \rangle$, and (c,g,k) isobath sur-
 1241 face area $A(z)$. The dashed black line shows the upwelling transport $\langle w \rangle A$ diagnosed directly from the simulated
 1242 velocity field. The solid black line shows the net watermass transformation, where its native density coordinate
 1243 has been mapped into a pseudo-depth coordinate by taking the average depth of a given buoyancy surface (eq.
 1244 19). For all of our simulations of abyssal circulations driven by near-boundary mixing, the Munk and Wunsch
 1245 (1998) expression is a poor substitute for watermass transformations, which themselves agree favorably with the
 1246 diagnosed vertical transport $\langle w \rangle A$.